

Multiple axon tracking
for biohybrid brain computer interfaces
from directional living neural networks

A thesis submitted for the degree of
Joint M.Sc. in Neural Systems and Computation UZH ETH
by Simon Steffens

Swiss Federal Institute of Technology Zurich, ETHZ
Dept. of Information Technology and Electrical Engineering, D-ITET
Laboratory of Biosensors and Bioelectronics, LBB

Examinor	Prof. Mehmet Fatih Yanik
First External Examinor	Prof. Janos Vörös
Second External Examinor	Tobias Ruff, Ph.D.

When I was One,
I had just begun.

When I was Two,
I was nearly new.

When I was Three,
I was hardly me.

When I was Four,
I was not much more.

When I was Five,
I was just alive.

Now I am Six. I am as clever as clever.
So i think I'll be six now for ever and ever.

Now We Are Six. By A. A. Milne

1 Abstract

Conventional brain computer interfaces of the last decades have relied on metal electrodes to interface biological neural systems. Whilst advances in electrode technology have enabled an exponential rise in single-neuron recording bandwidth, progress on the ability to electrically stimulate multiple single neurons *in vivo* has been stagnating. To transition neuroscience from observing correlations to imposing neural activity at high bandwidth and spatiotemporal resolution, capable stimulation technology is indispensable. Inspired by *in vitro* neuroscience and tissue engineering, biohybrid technology presents a promising paradigm shift for potent long-term biocompatible neural stimulation. This work revolves around a biohybrid implant utilizing ectopically grown retinal ganglion cells (RGC) in a microfluidic system as living implantable electrodes. To enable high bandwidth and functionally independent stimulation channels, this work addresses directional RGC growth through our Polydimethylsiloxane (PDMS)-based micro structure designs. Using a machine learning based growth cone tracking model on confocal recordings of axonal outgrowth, we tested 21 micro structure designs for their directional convergence from RGC seeding nodes into the implantable output channel. We successfully identified micro structure designs that exhibited 4-2.5 times as many axons reaching the output channel versus neighboring nodes. On top of that, we conducted followup experiments specifically investigating axon guidance primitives and the effect of design paradigms on achieving uni-directionally connected cultures. These insights on engineering directional living neural networks may not only yield higher bandwidth biohybrid interfaces, but prove useful for functionally more sophisticated brain-on-chip models.

Contents

1 Abstract	3
2 Preface	8
3 Introduction	9
3.1 Biohybrid neural interfaces	9
3.2 Engineered directional neural networks	10
3.3 Multiple object tracking	12
4 Methods	13
4.1 Experimental procedures	13
4.1.1 Dish preparation	13
4.1.2 Poly-D-Lysine & laminin coating	13
4.1.3 PDMS micro structure design, fabrication & mounting	13
4.1.4 Retina dissection	14
4.1.5 Spheroid creation	15
4.1.6 Seeding PDMS micro structures	15
4.1.7 Timelapse recording & image acquisition	16
4.2 Data analysis	16
4.2.1 Timelapse datasets	16
4.2.2 Initial timelapse processing	17
4.2.3 Axon growth cone labelling	17
4.2.4 Timelapse data preprocessing	18
4.2.5 Growth cone detection model	18
4.2.5.1 Temporal context frames	18
4.2.5.2 Tiling	18
4.2.5.3 Detection output format	19
4.2.5.4 Training procedure	20
4.2.5.5 Data association	20
4.2.6 Directionality inference from tracking	21
4.2.7 Analysis of axon guidance primitives	22
5 Results	23
5.1 Tracking performance	23
5.2 Micro structure designs	23
5.3 Between dataset variance	24
5.4 Axonal viability across datasets & designs	25
5.5 Directionality in PDMS designs	27
5.6 Axon guidance design primitives	29
6 Discussion	31
6.1 Summary	31
6.2 Growth cone tracking	32
6.3 Directional PDMS micro structures	33
6.3.1 Micro channel width	33
6.3.2 Merging channels	34
6.3.3 Grwoth direction rescue loops	35

6.3.4	Bias of between dataset variance	36
6.3.5	Axon guidance primitives	37
6.4	Conclusion & Outlook	38
7	Supplementary Figures	39

List of Figures

1	DIV 17 biohybrid implant assembled on glass MEA	10
2	Growth cone tracking model overview	19
3	Growth cone tracking model performance	24
4	PDMS micro structure designs	25
5	Between dataset variance and axonal viability	26
6	Directionality in PDMS designs	28
7	Axon guidance primitives in micro structure designs	30

List of Supplementary Figures

1	Initial timelapse preprocessing steps	39
2	Labelled training data examples	40
3	Preprocessing effects on pixel intensity distributions	41
4	Methodology illustrations	42

List of Tables

1	RGC medium composition	14
2	Overview of timelapse recording data	16
3	Minimum cost flow hyperparameters	21

List of Abbreviations

AAV	Adeno-associated virus
CAD	Computer aided design
CLSM	Confocal laser scanning microscope
CNN	Convolutional neural network
CNS	Central nervous system
DBS	Deep brain stimulation
DI	Deionized
DIV	Days <i>in vitro</i>
dLGN	Dorsal lateral geniculate nucleus
GFP	Green fluorescent protein
IQR	Inter quartile range
LED	Light emitting diode
MEA	Multi electrode array
MOT	Multiple object tracking
MOTA	Multiple object tracking accuracy
PDL	Poly-D Lysine
PDMS	Polydimethylsiloxane
PBS	Phosphate buffered saline
RFP	Red fluorescent protein
R-CNN	Regions convolutional neural network

2 Preface

Understanding the human brain requires neuroscience to develop complexity reducing model systems that capture relevant functional, anatomical or chemical features. The evaluation of which abstraction level and thus model system is appropriate for answering key functional questions about the brain has long been a source of controversy. This discussion is fundamentally rooted in the tension between losing essential features in overly simplified model systems, and dealing with overwhelming complexity and low experimental throughput in model systems more closely resembling the human brain.

Although this work broadly employs *in vitro* model systems thus trading off resemblance to real brains for higher throughput and reduced complexity, it is not primarily motivated by a certainty that this high abstraction level will indeed *solve* fundamental neuroscientific questions. Instead, this project aims to follow an approach that has led to notable progress in other domains, most prominently artificial intelligence: Developing an understanding of the system by engineering it. This method has found adoption in domains as neuromorphic engineering (Mead 1989) and neural engineering (Durand 2006), with the latter focusing i.a. on building technology from living neural systems. Guided by the engineering problems, the hope of these domains is that relevant neuroscientific questions are answered along the way. And even if this does not come true, advancement in these fields may still result in useful new technologies. The science presented here follows this pursuit.

3 Introduction

3.1 Biohybrid neural interfaces

Neuroelectric interfacing based on metal electrodes has made remarkable progress over the last decades (Maynard, Nordhausen, and Normann 1997, Jun et al. 2017). These technologies excel at locally confined high resolution neural recording for a time period on the order of weeks. However, given the immense challenges related to high quality neural interfacing (Stevenson and Kording 2011), naturally, existing recording and particularly stimulation technology exhibit shortcomings. The clinically most adapted CNS stimulation method, deep brain stimulation (DBS), does not specifically depolarize single neurons but instead exerts various modulatory effects on entire brain areas (Herrington, Cheng, and Eskandar 2016). Low spatiotemporal resolution may be tolerable for common DBS applications, however, addressing the clinically highly relevant cases of vision-, touch-, or hearing loss is currently limited by insufficient resolution (Tong et al. 2020). Another issue affecting both stimulation and conventional neural recording systems is the induced foreign body response. Due to natural brain movement, rigid metal electrodes cause inflammation, neuronal cell death and glia formation while simultaneously, conventional electrode insulation undergoes biodegradation resulting in decreased impedance (Tresco and Winslow 2011, Saxena et al. 2013, Grill, Norman, and Bellamkonda 2009, Polikov, Tresco, and Reichert 2005). In research applications, central nervous system (CNS) stimulation is most commonly performed through optogenetic tools (Zemelman et al. 2002, Boyden et al. 2005). While the cell-type specificity of optogenetics can be of great value, the limitations in spatial resolution inherent to *in vivo* light-based technology seem to be a major hurdle for increasing spatial resolution. On top of this, the risk of genetic off-target effects and adeno associated virus (AAV) immune responses restrict medical use cases in the near term (Mendoza, El-Shamayleh, and Horwitz 2017).

Biohybrid implants take a fundamentally different approach to neural interfacing, drawing inspiration from tissue engineering and *in vitro* neuroscience. First described by Stieglitz et al. 2002, this promising technology aims to solve the latent issue of biocompatibility by moving towards the integration of biological components (Rochford et al. 2020). At the same time, biohybrid technology may benefit from the highly impressive *spec sheet* of a neuron, including energy efficiency, self-containment, and signal transmission properties. Whilst engineering with neural tissue presents almost daunting challenges, the biocompatibility prospects of biohybrid interfaces are currently inaccessible by competing technologies. CNS applications of the biohybrid approach include the coating of metal electrodes with host cells (Purcell et al. 2009, Faveri et al. 2014), and the use of ectopic axons as electrodes (Tang-Schomer et al. 2014, Adewole et al. 2021). The currently most advanced biohybrid implant is based on a hydrogel microcolumn containing ectopic cortical axons that are optogenetically driven through a light emitting diode (LED) optical fiber outside the brain (Adewole et al. 2021). While synapse formation was shown anatomically *in vitro*, the *in vivo* proof-of-concept implantation did not go as far as showing functional target tissue innervation.

Current biohybrid implants trade off biocompatibility for interface bandwidth and control. For example, the biohybrid implant presented in Adewole et al. 2021 relied on optically exciting the entire ectopically grown neural population, resulting in limited control of delivered stimulation. While this spatial resolution may be sufficient for specific

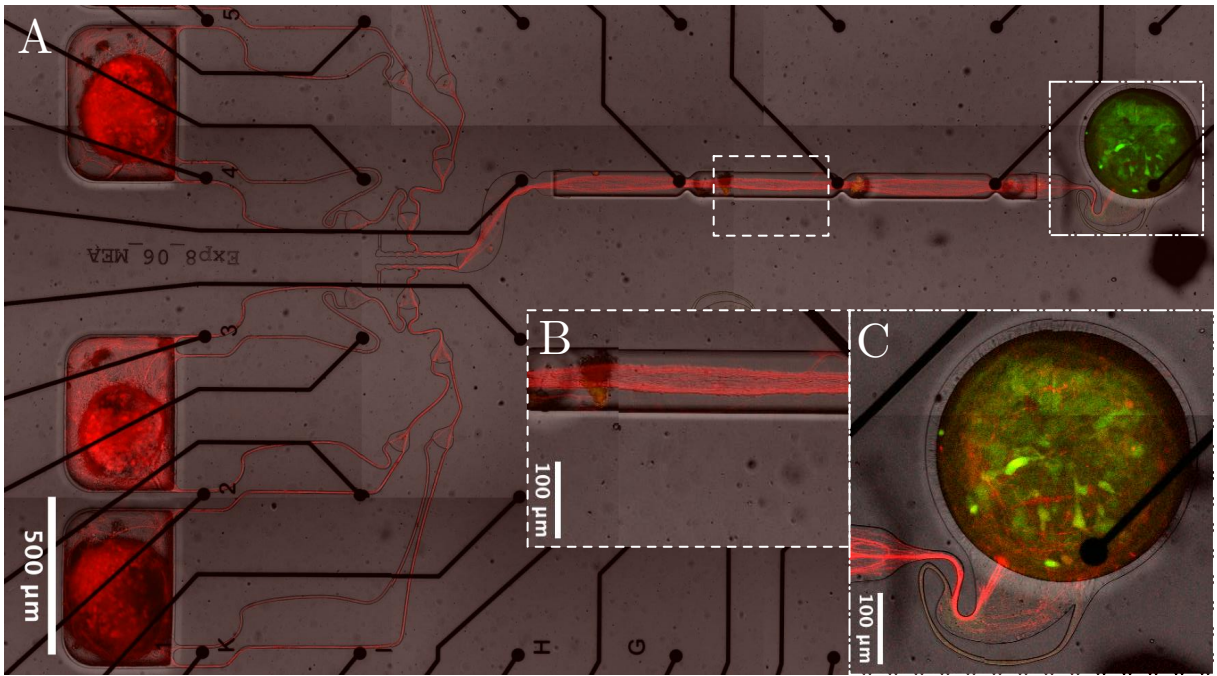


Figure 1: DIV 17 biohybrid implant assembled on glass MEA. **A** Confocal image of a biohybrid implant 17 days after seeding (DIV 17). Rat E18 RGC spheroids were labelled with mRuby (red), the E18 rat brain target was labelled with GFP (see Methods for details). Black lines in the transmission channel mark the PDMS micro structure. Only 3 of 4 RGC seeding wells are shown. **B** Magnification of the output channel with a grown nerve bundle. **C** Magnification of stomach target structure showing RGC innervation of E18 rat spheroid.

use cases, this implant design offers insufficient control for delivering high dimensional data, such as sensory input. For addressing the pressing issue of functionally restoring sensory modalities (Bourne et al. 2021), a biohybrid implant needs to allow for stimulating independent channels. To solve this crucial design requirement, the implant presented here is based on a PDMS micro fluidic system enabling the independent stimulation of axons grown in micro channels. Briefly, PDMS membranes are placed on coated glass dishes or multi electrode arrays (MEA) and seeded with E18 rat RGC spheroids (Figure 1 A). Axons extend through the 6 μ m high channel system until they reach the 3 mm long output channel which will eventually be implanted (Figure 1 B). The final device will utilise stretchable AuTiO₂ nanowire electrical contact pads for stimulating RGC axons (Tybrandt et al. 2018). Long term host cell survival will be ensured by having the implant face the brain surface such that RGC spheroids are integrated with the CNS microenvironment. The device will be implanted targeting the dorsal lateral geniculate nucleus (dLGN), although currently, the implant is optimized *in vitro* targeting E18 rat brain spheroids (Figure 1 C).

3.2 Engineered directional neural networks

It is well established that the connectivity within biological neural networks is a major determinant of the emerging electrophysiological dynamics. For example, the canonical microcircuit of the cat visual cortex exhibits a high degree of sparsity with predominantly local inhibitory-, and excitatory connections to achieve its output (Douglas and Martin 1991). Despite the general agreement on the significance of neural circuits, the vast ma-

jority of *in vitro* models remain limited to random connectivity schemes. Neglecting this property of *in vivo* neural networks may be well justified in studies that focus on basic biological properties, for example in response to drug admission. However, any model system investigating higher level functional properties emerging at the circuits-level (e.g. learning mechanisms) requires confined connectivity.

More elaborately controlled connectivity schemes are indispensable for technology relying on living neural circuits. Biohybrid interfaces as described above rely fundamentally on directional connectivity (Figure 1 A). Innervation of neighboring RGC source wells may result in activity dynamics independent of the imposed electrical stimulation pattern, rendering single stimulation channels or the entire device unusable. For this reason it is crucial for viable biohybrid implants to achieve high degrees of growth directionality. Likewise, more sophisticated models focusing on functional aspects of the peripheral nervous system (PNS) may benefit from directional *in vitro* models. PNS circuits generally show a pattern where sensory-, or motor axons converge to form a nerve that eventually diverges again in the target location. Building an *in vitro* platform resembling this architecture would be extremely useful for studying neuropathy, traumatic nerve injury, and tissue reinnervation. The canonical design of the biohybrid implant where multiple RGC source nodes converge into a common output channel replicates this motif.

The challenge of achieving directional *in vitro* networks is often reduced to imposing axonal or dendritic growth constraints once the neurons are seeded. Although it is conceivable that initially randomly connected neural networks develop directional connections solely by an electrically imposed activity pattern (Markram et al. 1997), this approach has so far been to no avail. Therefore, various *in vivo* inspired approaches have been taken to instead induce control on axonal outgrowth. Axon guidance mechanisms *in vivo* rely broadly speaking, on two categories of cues: structural and chemical ones (Weiss 1941, Goodman et al. 1984). Chemical cues have been employed for guidance by integrating substrate surface modifications favoring certain growth paths. Although many attempts are limited to micro patterning with PDL falling short of the highly complex chemical micro environment observed *in vivo*, still, a notable degree of axonal growth control is achieved (Yamamoto et al. 2016). While chemical guidance remains a promising direction for engineering defined neural networks in the future, structural guidance has shown more promising results at larger network scales (Forró et al. 2018).

The idea of utilizing structural growth guidance *in vitro* is largely based on advances in microfluidics for neuroscience (Millet and Gillette 2012, Neto et al. 2016). These platforms are commonly fabricated from PDMS, a polymer that can be molded at high resolution using soft lithography, while also exhibiting acceptable biocompatibility properties (Millet et al. 2007). 3D structural guidance principles are based on the inertia of growing axons, e.g. the inability to grow in sharp turns, and the tendency of axons to attach to edges (Francisco et al. 2007). These two findings are the basis of numerous PDMS design motifs proposed in the literature to achieve directional growth through PDMS micro structures: barbed-, and narrowing channels, (Feber et al. 2015, Peyrin et al. 2011,) redirecting hooks and consecutive arches (Pirlo et al. 2011, Na et al. 2017, Renault et al. 2016, Holloway et al. 2019), and diode-like triangles (Gladkov et al. 2017, Isomura et al. 2015). So far, the most competitive multi node directional networks are based on a relatively simple motif, where axons detach from sharp radii and thereby avoid growth in the undesired direction (Forró et al. 2018).

While Forró et al. 2018 presented respectable results for four-node-networks, the nerve model system and surely the biohybrid implant require an order of magnitude more nodes, while also deviating from the rather simple one-to-one connectivity scheme. In this work we present a high resolution screen on the growth directionality in 21 many-to-one PDMS designs. To the best of our knowledge, no networks have been shown to merge as many as 32 source nodes into a common target node. Since directional axon growth through PDMS micro structures is a probabilistic process, the addition of nodes increases the relative chance of non-directionally connected cultures.

3.3 Multiple object tracking

In this work, we employ a custom build, machine learning-based growth cone tracking model to screen PDMS micro structures for directional growth. Previous work has relied on screening network directionality electrophysiologically (Forró et al. 2018, Isomura et al. 2015, Feber et al. 2015), through calcium indicators (Na et al. 2017), manual-, or segmentation based axon counting (Pirlo et al. 2011, Forró et al. 2018) and by calculating fluoresce intensity ratios (Renault et al. 2016, Na et al. 2017). Due to the general geometrical complexity and the multitude of junctions within our micro structure designs, previously employed anatomically-based screening methods did not meet our requirements. Alternatively, functional screening methods offer high resolution, but are often limited to low experimental throughput. For those reasons, we resorted to tracking growth cones during the initial outgrowth phase, yielding a high resolution, anatomically-based estimation of directionality.

The problem of multiple object tracking (MOT) consists of identifying objects and linking their identities over multiple video frames, either offline with the entire sequence available, or online where future frames are not observed. Extensions of this include the classification and segmentation of identified objects. With notable exception (Braso and Leal-Taixe 2019), this problem has been divided into object detection and identity association. Since the seminal paper by Krizhevsky, Sutskever, and Hinton 2012 introducing the concept on learned convolution kernels, object detection has been increasingly dominated by machine learning based detectors. While the architecture of an image classifier is straight forward, mapping from the image pixel map to the number of classes, object detection deals with an unknown number of instances within an image, making it unclear what the network output shape should be. The first solution to this problem was the regions convolution neural network (R-CNN) architecture by Girshick et al. 2013, implementing the recurrent classification of small image regions (for improved versions see Girshick 2015, Ren et al. 2015). The inherently low inference speed in these architectures was addressed by the *you only look once* (YOLO) architecture by dropping the recursive aspect completely (Redmon et al. 2015, Redmon and Farhadi 2018, Long et al. 2020). The ensuing step of data association has been dominated by non machine learning based methods (Bewley et al. 2016, Kuhn 1955, Wang, Wang, and Yu 2019), although deep learning alternatives have recently been proposed as well (Wojke, Bewley, and Paulus 2017, Yoon et al. 2019).

In the biological microscopy literature, the above is often found under the term *particle tracking*, indicating the focus on small objects such as cells, organelles, or proteins (Tsai

et al. 2019, Anjum and Gurari 2020, Welshans and Bassell 2011). Although the general problem matches the outline above, tracking of biological objects such as growth cones generates a specific set of additional challenges. Concretely, the setup used for screening PDMS micro structures imposed the following: (i) Objects of interest, i.e. growth cones are often extremely small, thus conventional CNN architectures based on hierarchical feature extraction of larger objects are not suitable. (ii) Microscopy images are taken at very high resolution, raising computational demands. (iii) Inter frame intervals are long, here around 30 minutes, (iv) Growth cone appearance is highly variant; growth cones can overlap and collapse abruptly. (v) No labelled dataset exists, and widely available pretrained models generalize poorly. Our tracking implementation is build on established methods with modifications addressing the points i-v. For more details see methods 4.2.5.

4 Methods

4.1 Experimental procedures

4.1.1 Dish preparation

First, WillCo glass dishes ($\varnothing 30$ mm, WillCO Wells) were rinsed with acetone, isopropanol and ultra pure Water (Millipore Milli-Q System, $18M\Omega$), then dried with a nitrogen gun. Next, double sided adhesive rings were used to attach WillCo glass dishes to polystyrene dish frames. The assembled dishes were placed in a larger plastic dish with tape stripes preventing surface adhesion between dishes.

4.1.2 Poly-D-Lysine & laminin coating

The assembled glass dishes were coated using 1 ml Poly-D-Lysine (PDL) solution (56 $\mu\text{g}/\text{ml}$), incubating for 1-2 hours at room temperature. The solution was prepared using 1 ml of thawed up PDL stock (P7280, Sigma-Aldrich), and 8 ml of phosphate buffered saline (PBS) (10010015, Gibco, Thermo Fisher Scientific, Switzerland). After incubation, the PDL solution was removed and the dishes were washed 2 times with PBS, and once with deionized (DI) water to avoid salt crystal formation.

Subsequent to PDL application, dishes were coated with 10 $\mu\text{g}/\text{ml}$ laminin. This solution was prepared by slowly thawing 50 μl aliquots on ice, then adding 5 ml of NeurobasalTM plus (A3582901, Gibco). Between 300-800 μl laminin solution was applied to cover the whole surface of the glass dish. After 24h incubation at 37 °C, laminin solution was removed and the dishes were washed 1 time with PBS, and 2 times with DI water.

4.1.3 PDMS micro structure design, fabrication & mounting

PDMS micro structures were designed in a multi stage computer aided design (CAD) process. This was necessitated by the vast number of design motifs investigated in this study. Although not primarily intended for 2D CAD, Fusion360 (Autodesk, San Rafael, California) was used in the initial design stage. Fusion360 was chosen because of its powerful version control and design history system, enabling the natural integration of design

Component	Volume [ml]	Stored at [°C]
Neurobasal Plus (Gibco, A3582901)	237.5	4
DMEM (Gibco 11960)	237.5	4
Glutamax	5	4
Sodium Pyruvate (100mM, Gibco 11360-070)	5	4
Antibiotic-Antimycotic (100x, Gibco 15240096)	5	-20
N2 Supplement	5	-20
B27+ (50x)	10	-20
N21 Supplement (50x, R&D Systems AR008)	10	-20
NAC Stock (5 mg/mL)	0.5	-20
Forskolin Stock (4.2 mg/mL)	0.5	-20
BDNF Stock (50 µg/mL, Preprotech 450-02)	0.5	-20
CNTF Stock (10 µg/mL, Preprotech 450-13)	0.5	-80
NGF 7S Stock (10 µg/mL, final 10 ng/mL)	0.5	-80
GNDNF (10 ng/mL)	0.5	-20

Table 1: RGC medium composition. This medium was used throughout for culturing RGC neurons.

variables into the CAD workflow. Specific elements in different PDMS designs were inserted as separate components such that they could be updated independently from the base designs; for example the commonly used 2-joint motif. Single PDMS designs were then exported as .dxf files by projecting extruded bodies to 2D sketches. Importantly, the projection link had to be deleted to export valid .dxf files. The single PDMS designs were imported to AutoCAD (Autodesk, San Rafael, California) to define fabrication mask layers and arrange designs on the wafer. Finally, the wafer design was exported as a .dxf file and imported from KLayout where the final .gds2 file was generated. The wafer and PDMS designs were fabricated by Wunderlichips (Switzerland) employing standard soft lithography (for details see Forró et al. 2018).

The PDMS membrane delivered by Wunderlichips was separated into independent PDMS structures on a laser cutter (Speedy300, Trotec, Switzerland) using 8 % power at 14 cm/s. Subsequently, the structures were thoroughly rinsed with 70 % ethanol. For a subset of experiments, a PDMS frame was laser cut from 5mm thick cured PDMS. Using uncured PDMS, it was attached on the micro structure to enclose the output channel area. After curing for 1h at 80°C, they were picked up with a pair of surgical forceps and slowly placed on the coated glass dishes (see above). Importantly, prior to mounting, a thin film of DI water was put on the glass dishes to facilitate mounting without enclosed air bubbles. As the last dish preparation step, RGC medium (see composition in Table 1) was added and the dishes were desiccated for 30-60 minutes to remove air from the PDMS micro channels.

4.1.4 Retina dissection

Animal experiments were performed with highest of care maximizing animal welfare and following 3 R. The approval was obtained from Cantonal Veterinary Office Zurich, Switzerland under license SR 31175 - ZH048/19. E18 time-mated pregnant rats (Janvier Laboratories, France) were sacrificed and embryonic eyes were collected in Hibernate medium on

ice. Before retinal dissection, instruments were disinfected using 70% ethanol. Under a benchtop microscope (DFC420C with 4X magnification, Leica, Germany), eyeballs were pierced near the ciliary muscles using a sharp pair of forceps. This opening was carefully extended by inserting a second pair of forceps on which the sclera was subsequently striped off. Retinas were collected in Hibernate medium on ice after gently removing the lens and hyaloid vasculature.

4.1.5 Spheroid creation

To create RGC and thalamus spheroids, first, 500 μ l of AggreWellTM rinsing solution was added to the AggreWellTM 800 microwell plates. To ensure the absence of air bubbles in the microwells, the plate was centrifuged at 2000 g for 5 minutes or until no air bubbles were observed. Finally, the rinsing solution was washed away with Neurobasal medium and 1 ml of RGC medium was added to each of the micro wells.

For retina and thalamus dissociation, first, a solution was prepared by dissolving 50 mg BSA and 90.08 mg glucose in 50 ml of sterile PBS. 5 ml of this solution were vortexed with 2.5 mg Papain. After 30 minutes of incubation at room temperature, the Papain solution was filtered using a 0.2 μ m sterile filter and 5 μ l DNase were added. Tissues were dissociated by first incubating them for 15 minutes at 37 °C in 5 ml of this Papain solution. After 15 minutes, the Papain solution was carefully removed without disturbing the pallet. In three cycles, 5 ml of warmed Neurobasal medium were added, incubated for 3 minutes, then removed again. To suspend the retinas, 2 ml of RGC medium were added and repeatedly pipetted up and down using a pipette boy. After cell straining with a 40 μ m filter, the number of viable cells was determined using a Trypan Blue stain on a hemocytometer. To create spheroids of 3000 cells, the appropriate cell concentration to fill 300 micro wells was calculated and prepared. In order to obtain constant volumina across experiments, wells were filled up to 2 ml using RGC medium. Lastly, to color-label the spheroids, one μ l of mRuby virus (scAAV-DJ/2-hSyn1-chl-mRuby3-SV40p(A), hereafter called RFP) or GFP virus (scAAV-DJ/2-hSyn1-chI-EGFP- SV40p(A)) was added for adeno-associated virus (AAV) mediated transduction. The AggreWellTM plate was then centrifuged at 100 g for 3 minutes to fill the microwells with cells. After confirming even cell distribution and expected spheroid sizes, the plate was placed in the incubator at 37 °C with 5% CO₂ for 16-20 hours.

4.1.6 Seeding PDMS micro structures

To remove the virus before seeding, spheroids were pipetted out of the AggreWellTM plate into a small petri dish and carefully washed in Neurobasal three times. Under the benchtop microscope, around 50 spheroids were pipetted from the petri dish into the prepared micro structure dish (see 4.1.3). They were then carefully placed in the appropriate location within the PDMS micro structures using a pair of micro scalpels. Timelapse structures were either additionally seeded with thalamus spheroids or small thalamic tissue pieces were placed on top of the PDMS micro structure output channel. After 10 minutes of seeding, the culture was transferred back to the incubator for 5 minutes to recover the pH. Once all seeding spots were filled, the culture was placed in the incubator at 37 °C with 5 % CO₂. Half the RGC medium was exchanged every 3-4 days.

4.1.7 Timelapse recording & image acquisition

Both timelapse,- and single images were recorded on an inverted confocal laser scanning microscope (CLSM) (FLUOVIEW FV3000, Olympus). Timelapse recordings were performed using a 20x objective, 800 μm pinhole, a gain of 580-600 V, and laser power of 0.8-1 %. The axonal growth in each of the approx. 40 PDMS micro structures was captured by 2 x 4, 1024x1024 tile scans, resulting in an optical resolution of 0.49 μm , and a pixel size of 0.62 μm . Absorption and emission spectra of fluorescent markers were set according to the manufacturers recommendations. To maintain cell viability throughout the recording, the integrated incubator chamber was setup to 37 °C with 5 % CO₂. Fast solid state storage media was used to prevent a frame rate bottleneck from an insufficiently fast network connection.

Single images were acquired under the same settings, except that a 10x objective was used. This resulted in an optical resolution of 0.88 μm and a pixel size of 1.24 μm .

4.2 Data analysis

4.2.1 Timelapse datasets

This work incorporates three PDMS micro structure timelapse recordings that were acquired at different timepoints. Accordingly, the data used in this work is based on three experiments, where each experiment was performed with 8-14 rat embryos (compare 4.1.4 for details). One of the three timelapses was solely obtained for generating model training data, thus the presented results are based on two experiments with a total of 16-28 biological replicates. A summary of timelapse datasets is given in Table 2.

We treat each half of a PDMS micro structures as independent samples, as all designs are strictly symmetric around the output channel. Given that the two experiments included each design in duplicate, a maximum of 8 samples per design were obtained. However, since fabrication failure within designs, bad tracking performance, and overly strong undergrowth led to discarding samples, few designs are limited to a sample size of $n = 4$.

	Acquired	Setup	T [min]	n frames	Length [days]	Model usage
Dataset1	20.12.20	1 design	40	37	1	Training
Dataset2	27.08.21	2 designs, chamber	31	210	4.5	Training
Dataset3	27.10.21	18 designs, chamber	31	210	4.5	Inference
Dataset4	07.10.21	21 designs, stomachs	32	242	5.4	Inference

Table 2: Overview of timelapse recording data. *n designs* refers to the number of unique PDMS micro structure designs composing the dataset. *Chamber* setups employed large thalamic tissue pieces enclosed by a PDMS frame for concentrated attraction cues (see 4.1.3 for details). *Stomach* setups omitted PDMS frames and instead seeded a thalamic spheroid in the target well (see Figure 1 C). T refers to the temporal period of the recording. White space between rows indicates different experiments.

4.2.2 Initial timelapse processing

The proprietary `.oir` files produced by the CLSM were converted to three dimensional `.tif` files using Python's `bioformats` package, which relies on a java virtual machine implemented within the `javabridge` package. Additionally, `.tif` frame sequences were rendered to `.mp4` video using `scikit-image` and `open-cv` (Suppl. Figure 1 A). These videos were used for initial evaluation of the timelapse, validating for example absence of strong undergrowth and artifacts. The transmission channel of each PDMS micro structure timelapse was then loaded into napari, a python based n-dimensional image viewer (Sofroniew et al. 2021). Using `skimage.filters` to segment the micro channels in the PDMS designs, edge magnitude was detected with `prewitt()`, gaussian smoothing was performed with `gaussian()` ($\sigma = 1$), thresholding was done with `threshold_otsu()`, and finally, the segmentation was cleaned up using `skimage.morphology.binary_closing()` (diameter = 4) (Suppl. Figure 1 B). Subsequently, the segmentation of the PDMS micro channels was manually cleaned up, mainly using the bucket tool to fill areas enclosed by detected edges. To remove patches in the mask, the target point of the PDMS design was labelled and used as the origin to perform `skimage.segmentation.flood()`. To recognize specific axon locations, both the final output channel and the first 100 μm of the channels exiting the source wells were segmented and saved as binary masks (Suppl. Figure 1 C).

4.2.3 Axon growth cone labelling

The axon growth cone tracking model was trained using Dataset1, and Dataset2 which included timelapse recordings of three unique PDMS designs (compare Table 2). The labelling of these three image sequences was performed by one human expert using the napari image viewer. The workflow for obtaining the four dimensional label of `FrameID - AxonID - X coordinate - Y coordinate` was as follows:

1. Load timelapse sequence.
2. Create empty set of axon identities.
3. Inspect short time slice of 3-6 frames for distinct, coherently moving blob.
4. Identify axon identity by its growth cone.
5. Trace axon identify over adjacent frames until unidentifiable.

In the scenario where two separate growth cones converge forming a single observable growth cone, one of the two identities was arbitrarily chosen to be continued while the other one was terminated. Hence, the underlying number of axons for a given growth cone label may be larger than one. It should also be considered that there is some degree of uncertainty in the ground truth labels. Especially when the PDMS micro channels become largely filled, distinguishing between GFP-protein trafficking along existing axons versus new growth cones becomes challenging. The annotations here were consistently done more conservatively, weighting the avoidance of false positives higher than missing true positives. Following this conservative labelling methodology, an axon identity was only considered if it appeared over more than three frames. From three concatenated PDMS micro structure timelapses, 300 growth cones were identified over N=327 frames where the average axon identity lifetime was 24 frames. Four labelled example frames are shown in Suppl. Figure 2, and an overview of the axon identify lifetime is given in Suppl. Figure 4 A.

4.2.4 Timelapse data preprocessing

The CLSM 12bit gray scale intensity values saved as 16bit unsigned integers were first converted to a scale of 0 to 1 using `skimage.util.img_as_float()`. For image sequences that had an offset in the intensity profile, this offset was subtracted such that the minimal intensity was always 0. Next, the segmentation of the micro channels was used to mask the image sequence (see Suppl. Figure 1 C for an example mask). The resulting initial distribution of intensity values for two example training and inference frames are shown in Suppl. Figure 3 A top left. In the next step, intensity values below threshold = 0.00083 were clipped and set to 0 (top right). Then, the intensity profile I_{in} was stretched using `skimage.exposure.adjust_log()` function with a gain $g = 1$ which transformed the distribution according to formula 1 (bottom left).

$$I_{out} = g * \log(1 + I_{in}) \quad (1)$$

Finally, the intensity distribution was divided by the global standard deviation across the entire training image sequence, ensuring unit variance in the model input data (Suppl. Figure 3 A, bottom right). Both frame-wise, and mean-based standardizations were omitted since their application resulted in decreased detection performance. The intensity distributions from train- and inference data do not overlap in Figure 3 A because the sparsity differs vastly across frames. Train intensity values do not increase from t_0 to t_N because t_N corresponds to a different timelapse video (Dataset2) which is more sparse than t_0 (Dataset1).

4.2.5 Growth cone detection model

4.2.5.1 Temporal context frames

The growth cone detection model implemented in PyTorch follows the general approach of YOLO (Redmon et al. 2015) where the detections are obtained by a single pass through the network (Figure 2 A). The first aspect in which it deviates from the original is that instead of inputting an RGB image, the network receives a temporal stack of five gray scale images. Concretely, to detect growth cones at frame t_0 , frame $t_{-2}, t_{-1}, t_0, t_1, t_2$ are fed into the network. This architecture aims to imitate the strategy of human labelling: by inspecting single frames, growth cone identification is highly uncertain; only when scanning sequences of frames, coherently moving blobs of particular shape and dynamics can be linked to growth cones and thus an axon identity. To always provide full temporal context, frame t_0, t_1, t_{N-1}, t_N were omitted from detecting growth cones in the image sequence. Computing the motion between frames manually by subtraction yielded decreased detection performance over the implicit approach of passing temporal context frames. An illustration of the motion computation is shown in Figure 2 B.

4.2.5.2 Tiling

Each yellow block in Figure 2 A represents a sequence of 2D-convolution, batch normalization (Ioffe and Szegedy 2015), and Leaky ReLU (Maas, Hannun, and Ng 2013). Orange layers stand for maximum pooling operations. As performing detection on the original resolution of 3868 x 1972 was computationally intractable, the timelapse frames were split into 512 x 512 tiles (see Figure 2 B and grid in Suppl. Figure 2). The CNN computes a convolutional feature map of 16 x 16 x 160, thus a single *feature pixel* represents a

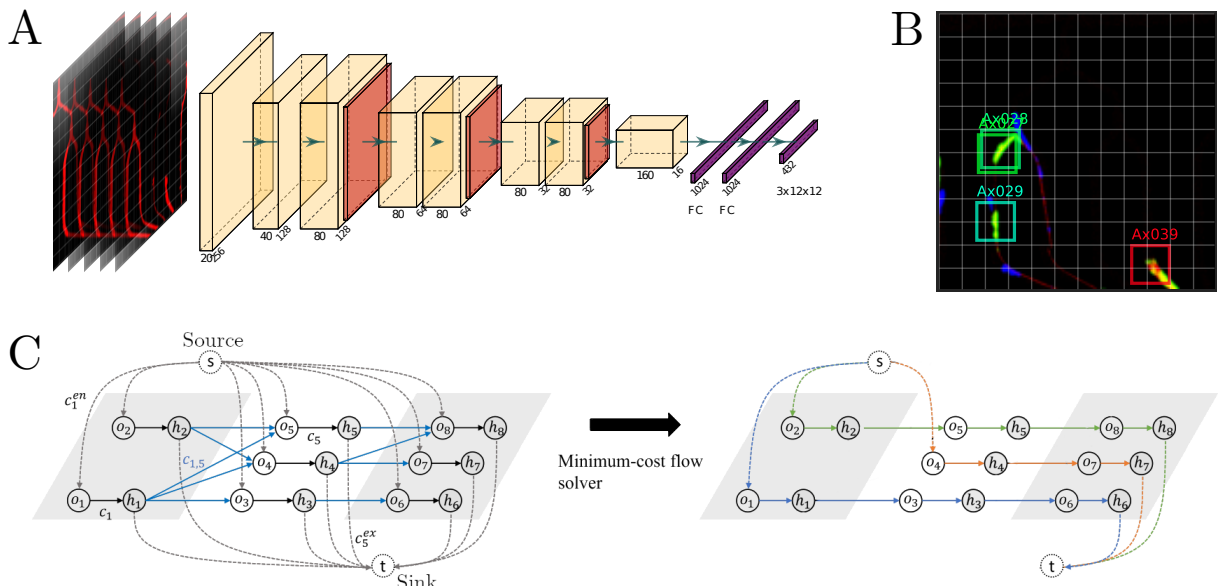


Figure 2: Growth cone tracking model overview. **A** CNN architecture. Each yellow block in represents a sequence of 2D-convolution, batch normalization (Ioffe and Szegedy 2015), and Leaky ReLU (Maas, Hannun, and Ng 2013). Orange layers stand for maximum pooling operations. FC stands for fully connected layers. **B** Example tile illustrating the YOLO label format. Each grid box can be predicted to contain a growth cone. In this example, 4 of 12 x 12 grid boxes are positive. Green colors in the tile represent positive motion (pixel intensity increased from frame t_0 to t_1), blue represents negative motion. Grid box size = 26 μm . **C** Minimum cost flow optimization illustration adopted from (Wang, Wang, and Yu 2019). Frames are illustrated in gray and white background, detections within a frame are represented by a pre- (o_i), and post (h_i) node. Blue edges on the left represent costs between detections in adjacent frames. Coloured edges on the right indicate identity associations after solving the graph.

region of $\frac{512}{16} = 32$ pixels in the original 512 x 512 input image. The CNN output resolution was a relevant consideration for its architecture, as the detection objects of interest are small and potentially locally clustered (using microscopy settings described in 4.1.7, growth cones are between 4-26 pixels). If the same CNN feature output resolution was to be achieved using original timelapse frames, the CNN output would be of shape of $\frac{3868}{32} \times \frac{1972}{32} \times 160 \approx 120 \times 61 \times 160$. Storing the weights between this high-resolution CNN feature map and the first fully connected layer exceeded GPU memory. An additional computational benefit is achieved by skipping empty tiles. From visual inspection, the discontinuities between tiles did not seem to result in decreased detection performance for growth cones near the tile edges.

4.2.5.3 Detection output format

Following the general YOLO label format, the network is trained to find a mapping from a single tile CNN feature map to a $12 \times 12 \times 3$ array. Here, the first two dimensions represent a grid of the input tile, the last dimension refers to the confidence of the respective grid box containing a growth cone, and X-, Y grid box coordinates referring to the relative location of a growth cone within the box (Figure 2 B). This representation results in the limitation, that only one growth cone can be detected per grid box. As the example in Figure 2 B shows, close growth cones may still be detected as two separate identities if their centers are located in different grid boxes. In the worst case scenario, the spatial

detection resolution of multiple growth cones is limited by the grid box size which is equal to $\frac{512}{12} = 43$ pixels or $26 \mu\text{m}$. This resolution was sufficient for the application of our model as densely grouped growth cones were the exception.

To drop overlapping detections, non max suppression was applied to the final detection output according to (Bodla et al. 2017) using a minimum euclidean distance of 23 pixels.

4.2.5.4 Training procedure

The training data was split into 287 train frames (0.87), and 40 (0.13) consecutive test frames which spanned two different PDMS micro structures. The final model used for inference was trained on the entire dataset. Using translation, rotation, horizontal and vertical flipping as data augmentation, the model was trained up to convergence for 1000 epochs (Figure 3 A). The loss function below (2) is a slight modification from the original.

$$\lambda_{anchor} \sum_{i=0}^{S^2} \sum_{j=0}^B \mathbb{I}_{ij}^{obj} [(x_i - \hat{x}_i)^2 + (y_i - \hat{y}_i)^2] + \lambda_{obj} \sum_{i=0}^{S^2} \sum_{j=0}^B \mathbb{I}_{ij}^{obj} (c_i - \hat{c}_i)^2 + \lambda_{noobj} \sum_{i=0}^{S^2} \sum_{j=0}^B \mathbb{I}_{ij}^{noobj} (c_i - \hat{c}_i)^2 \quad (2)$$

where $S = 12$ is the number of tiles, $B = 1$ is the number of detections per grid box, \mathbb{I}_{ij}^{obj} equals to 1 if a growth cone exists, 0 otherwise, \mathbb{I}_{ij}^{noobj} equals to 0 if a growth cone exists, 1 otherwise, c_i refers to the confidence that an object exists in the grid box, and x_i, y_i represent the grid box coordinates. $\hat{\cdot}$ stands for the ground truth label. The loss terms for predicting coordinates, object presence, and object absence are weighted according to $\lambda_{anchor} = 45$, $\lambda_{obj} = 54.25$, and $\lambda_{noobj} = 0.75$ respectively. The balancing of those terms is based on the proportion of positive grid boxes which is $\approx 0.7\%$. The initial learning rate was set to 0.0005 and decayed with the rate γ given in formula 3.

$$\gamma = e^{-\frac{1}{10}\sqrt{x}} \quad (3)$$

where γ is multiplied with the original learning rate, and x refers to the current epoch. Pytorch’s Adam optimizer (Kingma and Ba 2014) was used for fitting the model with $\beta_1 = 0.9$, $\beta_2 = 0.999$.

4.2.5.5 Data association

The implemented growth cone tracking model follows a classical object tracking paradigm of splitting the problem into object detection and identity association. For this second step, the detections produced by the YOLO-like architecture need to be classified into unique growth cone identities that live over several video frames. In this work, identity assignment is framed as a graph problem where we seek minimum cost flow solutions (Wang, Wang, and Yu 2019). At a high level, nodes represent detections at particular frames, and edges represent identity associations between them (see illustration in Figure 2 C). Each detection confidence is also represented as an edge, which elegantly incorporates the detection model uncertainty into forming identity trajectories through the graph and avoids the setting of explicit detection confidence thresholds. At the basis of associating detections between frames is the cost we assign between them. This cost can be interpreted as the likelihood the two detections correspond to the same growth cone identity. In contrast to other domains where visual similarity is highly relevant, because of the large morphological variance, the edge costs here are completely based on the spatial distance

between detections. Specifically, the A* distances (Hart, Nilsson, and Raphael 1968) between detections computed on the segmented PDMS micro channel mask using a custom C++ implementation. This cost considers the constraint, that growth cones can only translocate within the micro channels and are limited in outgrowth speed. Solving the graph optimization problem includes the constraint, that a node can only receive and emit a single edge, or in other words, a node can only represent a single identity. As shown by Wang, Wang, and Yu 2019, the graph can be solved optimally and efficiently using integer linear programming. The implementation here is based on the open-source package `libmot`, using the build-in `MinCostFlowTracker`. The optimal hyperparameters listed and explained in table 3 were identified with a grid-search algorithm on test data (see Figure 3 D).

Edge cost threshold	Entry-exit cost	Miss rate
0.7	2	0.6
Maximum number of misses	Minimum network flow	Maximum network flow
1	5	450
Visual similarity weight	Confidence capping method	
0	<i>scale</i>	

Table 3: Minimum cost flow hyperparameters. The edge cost threshold determines if an edge is pruned or kept, the entry-exit cost defines the cost of creating and terminating identities, the maximum number of misses indicates for how many frames an identity can be not detected, but still not terminated, the miss rate determines how much cost is incurred from missing detections (low means high cost), minimum and maximum network flow gives the minimum and maximum number of identities over all frames, visual similarity weight determines the degree to which visual similarity between detections contributes to the cost, and finally the confidence capping method sets the behavior for confidence values above 1, where *scale* means normalize to maximum confidence.

4.2.6 Directionality inference from tracking

Using the growth cone trajectories that lived at least for 5 timepoints, the degree of directional growth through the PDMS micro structures can be inferred. Analogous to the identity association cost employed for formulating the graph, directionality inference also relies on computing A* paths on the micro channel segmentation mask. For each detection that composes the growth cone trajectory, we compute the shortest distance to a human-labelled target point located in the output channel (see Suppl. Figure 1 C). Our PDMS designs have the property, that the shortest path towards this point is precisely the desired growth path. More intuitively, the desired growth path towards the output channel has no detours. Thus, we can employ the A*-shortest path towards the output channel as a proxy for confirming the correct growth direction through the micro channels. Concretely, a correctly growing axon should exhibit constantly decreasing A* distances towards the output channel. Conversely, any increase in distance indicates growth in the undesired direction.

A variety of metrics were considered for evaluating the degree of directional growth through PDMS micro structures. Δ distance-to-output channel of each axon provides a large sample size, but axon track length is not the most direct metric of interest. To circumvent the bias of long axon tracks, we count the number of correctly- and incorrectly growing axons, as the basic property of growth direction is more relevant than the overall covered distance. However, since this counting overvalues slow forward growth with little convergence to the final target location, we also analyse the number of axons reaching a neighbour, and the output channel, respectively. Preferably, we would rely solely on this metric, however, with the limited timelapse duration of around 5 days, many structures exhibit a very low number of axons reaching target and neighbours which reduces the sample size significantly. For this reason, this metric was only employed for qualitative measures. To obtain a final metric incorporating both forward convergence and backwards avoidance, we compute the smoothed directionality ratio δ of the two axon counts (Equation 4).

$$\delta = \frac{n_{target} + 1}{n_{neighbor} + 1} \quad (4)$$

where n_{target} and $n_{neighbor}$ refer to the number of axons reaching the output channel and a neighbour, respectively. One is added to both quantities to first, avoid discarding samples with no cross-growth, and second to lower the weights of small axon numbers. Intuitively speaking, the addition becomes negligible for large values, while reducing fold-differences of small, and thus potentially more uncertain counts. Alternative methods, for example normalizing to the sum of the two counts elicit less distinct differences between groups.

4.2.7 Analysis of axon guidance primitives

Data for this experiment included 16-28 biological replicates split in two experiments, one of which was imaged at DIV 7 and 14, the other only at DIV 14. The investigation of axon guiding design primitives relied on specific PDMS micro structure designs each aimed at answering a specific question. In most cases, these designs incorporated a source seeding node from which RGC axons extended to a growth decision point. Different features were implemented in the designs to bias the growth towards a specific channel. Since the segmentation of single axons within each channel was out of scope for this work, the median fluorescence intensity within the micro channels prior and post the decision point was employed to estimate the number of present axons. To compute the growth bias at a decision point, the ratio of median intensities was computed according to equation 5. Since high pixel intensities likely translate into more axons, we duplicated the computed bias metric β at a particular motif according to the pixel intensity in the inlet micro channel. This weighting of more filled channels described in formula 6 and 7 resulted in less outliers.

$$\beta = \frac{I_{bias} - I_{unbias}}{I_{bias} + I_{unbias}} \quad (5)$$

$$S = \{\beta, \dots, \beta\} \quad (6)$$

$$|S| = n_{duplicates} = \begin{cases} \left\lfloor \frac{I_{inlet}-\theta}{\alpha} \right\rfloor + 1 & \text{if } I_{inlet} < 6\alpha - \theta \\ 6 & \text{otw.} \end{cases} \quad (7)$$

with I_{bias} , I_{unbias} , and I_{inlet} describing the median pixel intensity in approximately 50 μm of the biased channel, the unbiased channel and the inlet channel, respectively. S refers to the set of duplicated bias measurements β whose cardinality is defined by the input intensity described in formula 7. The duplication depends on the minimum threshold intensity $\theta = 0.04$, and the step intensity $\alpha = 0.06$. A visualization clarifying the analysis methodology is shown in Suppl. Figure 4 C, D and in the results, Figure 7.

5 Results

5.1 Tracking performance

The presented model splits the tracking problem into growth cone detection and identity association. A representative example of detections is shown in Figure 3 B. Given the temporal stack of five image tiles, the detection model accurately identifies growth cones in PDMS micro structure timelapse frames. False positive detections made by the model are often ambiguous image regions that may be interpreted as positives under less conservative ground truth labelling. On the test set, the detector reaches a precision of 0.73, and recall of 0.79. F1 score at a confidence threshold of 0.79 is 0.76 (Figure 3 C). A both deeper and wider CNN architecture did show decreased performance. The ensuing step of identity association was performed in a graph framework optimizing for minimum cost flow solutions. Matching detection performance in tracking is challenging as in addition to detection, identity switches, object occlusions, and suitable identity creation-, and termination need to be considered. Using the multiple object tracking benchmarks proposed in Leal-Taixé et al. 2015, our tracker achieves identity precision, recall and F1 score of 0.73, 0.68, 0.71, respectively, which is a reasonably small drop from detection performance (Figure 3 D). The commonly used MOTA (multiple object tracking accuracy) metric which considers the number of false positives, false negatives (including identity), and identity switches normalized to the number of ground truth labels was 0.61. A more intuitive measure of tracking performance is visualized by the top bar in Figure 3 D, indicating the proportion of growth cones mostly tracked (0.57), partially tracked (0.23), and mostly lost (0.2).

Although not utilized for our application of the tracking model, axons can be reconstructed from the growth cone track, assuming that outgrowth followed the shortest path between detections. A visualization of the reconstructions is shown in Suppl. Figure 4 B.

5.2 Micro structure designs

The tracking model described above was used for evaluating a set of 21 PDMS micro structures designed for directing axon growth from multiple source regions towards a common target. These designs are the result of unpublished previous work extensively described in Supplementary Information 1. In short, the 21 designs test a set of presumably relevant variables that yield directional axonal growth, including different types of 2-joints, joint

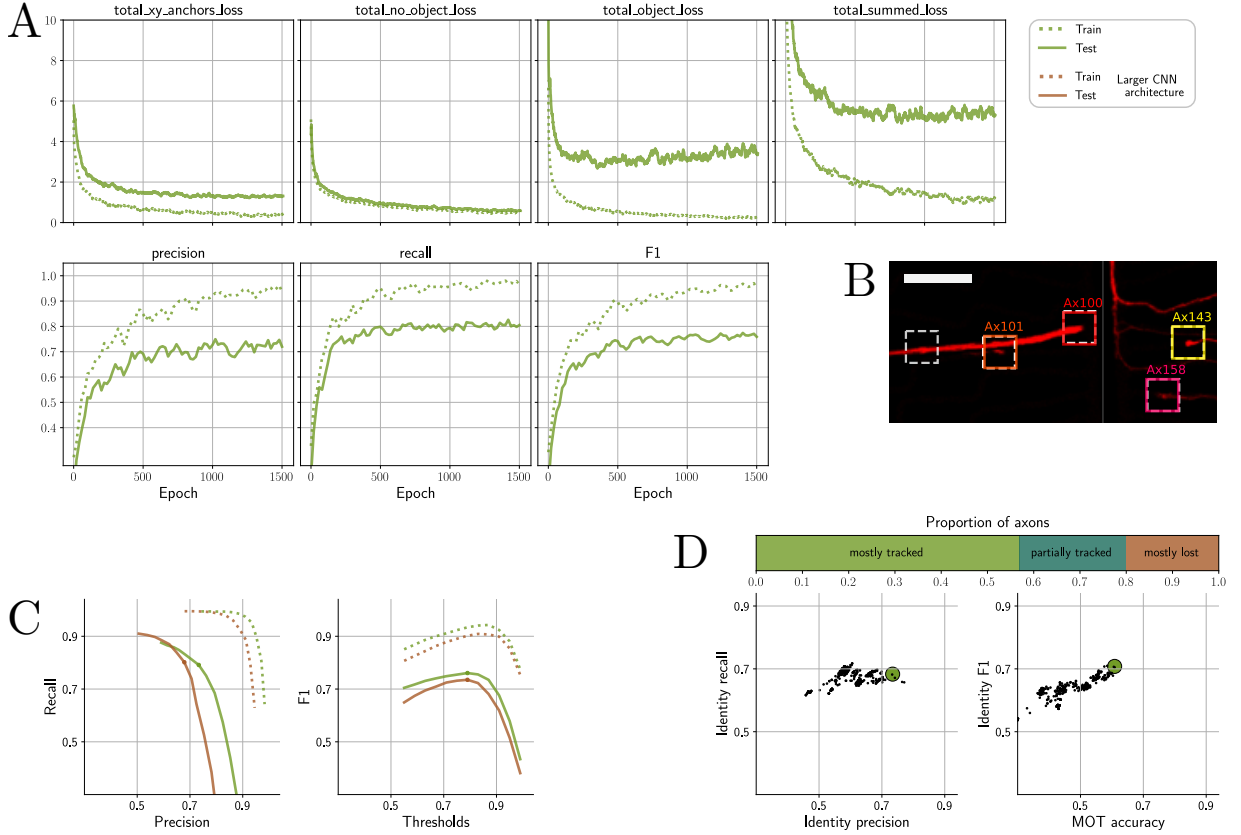


Figure 3: Growth cone tracking model performance. **A** Loss and performance over 1500 training epochs. Dotted line refers to train set, solid line to test. The plotted loss was smoothed with an exponentially decaying kernel over 25 epochs, precision, recall, and F1 over 60 epochs. **B** Representative growth cone detection example. Dashed boxes are predicted, colored ones are ground truth. Scale bar = 90 μm . **C** Detection performance. The maximum F1 score for varying confidence thresholds on test set is indicated by the dot. The brown line shows performance for a model with wider and deeper architecture. Legend in A applies. **D** Model growth cone tracking performance. Identity precision and recall incorporate classification of correct identity. Each black dot represents the performance using one set of hyperparameters, the green dot represents the highest scoring set (see Table 3) where identity F1 was 0.71, MOT accuracy 0.61. MOT accuracy measures the number of false positives, false negatives, and identity switches normalized to the number of ground truth labels. The top bar visualizes the proportion of growth cones that were mostly tracked (green, >80% identity lifetime tracked), mostly lost (brown, <20%), and partially tracked (dark green, between 20-80%).

placements and joint frequencies. Figure 4 illustrates the specific features implemented in the different designs. Design 05 on the right exemplifies the general PDMS architecture composed of four source wells, the final lane, the higher output channel with added diffusion wells and finally a target stomach (Forró et al. 2018).

5.3 Between dataset variance

The translocation of RGC growth cones was tracked over a period of five days to infer the degree of directional growth through new PDMS micro structure designs. The directionality was evaluated based on the A^* distance-to-output channel over time (see Methods 4.2.6). Figure 5 A shows this inference of directionality from output channel distances for tracking axons in Design 05. Axons that grow towards the output channel exhibit

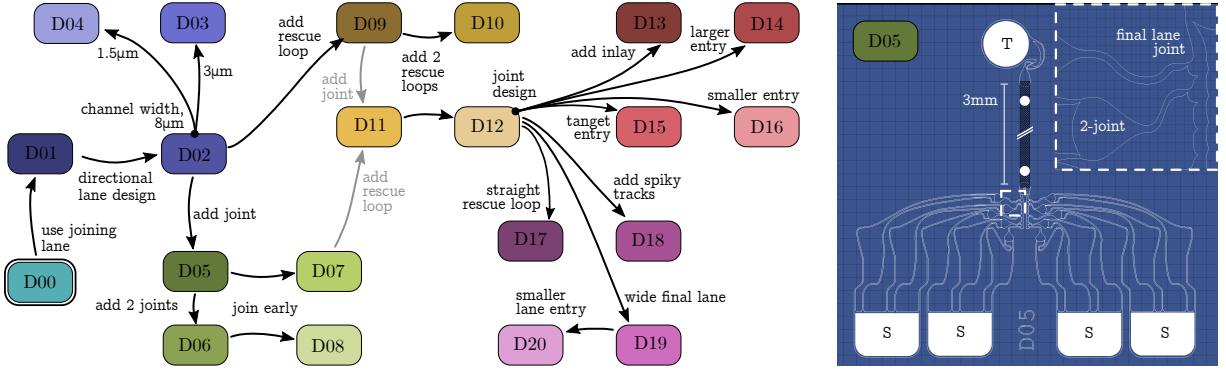


Figure 4: PDMS micro structure designs. The left illustration provides an overview of the 20 modelled micro structures including their distinguishing design features. Starting from Design 00 (D00), the arrows can be interpreted as an implemented design change. For example, D05 and D06 differ specifically in the number of 2-joints. For more details on the single designs see Suppl. Information 1. On the right, the D05 design is shown as an example. Filled white regions are openings, white lines indicate 6 μ m high channels, the black region represents the 75 μ m high output channel (note discontinuity for illustrative reason). RGC spheroids are seeded in the source wells (S), the thalamic attractor is placed in the target well (T). Grid dimension 100 μ m. The magnification highlights the two main merging structures, 2-joints and final lane joints.

smaller distances over time, thus the Δ distance towards the output channel is negative for directionally growing axons. These distances form the basis of subsequent analysis steps.

Tracking was performed on two datasets obtained from experiments with slightly differing setups. While Dataset4 was acquired using thalamus spheroids placed in stomachs (see Figure 4 right), Dataset3 used free floating thalamic tissue pieces enclosed by PDMS frames to locally increase attractor concentration. Dataset3 and 4 exhibit a collection of significant differences. Figure 5 B highlights the variation of growth directionality between the two. During the initial outgrowth phase, Δ distances collectively decrease for all designs by 300 μ m in both datasets. Albeit with increasing variance, this average distance is kept throughout, indicating a dominance of non-moving growth cones. While the averages are comparable, the variance of directionality differs vastly between Dataset3 and 4. In contrast to Dataset3, Dataset4 shows only marginal differences between designs, and the overall variance is smaller. This discrepancy is condensed in Figure 5 B (right) with the temporal dimension collapsed. To better identify differences in directionality between designs, subsequent analysis was conducted on the interval with maximum variance, DIV 3.5 to 6 (see dashed line).

5.4 Axonal viability across datasets & designs

PDMS micro structure designs primarily focus on achieving directional growth towards the output channel. While this metric is crucial, as with any metric, ignoring other relevant factors may result in poor overall performance. In our case, these other relevant factors are indicators of neural viability, including axonal outgrowth velocity, frequency of outgrowth, long-term survival and electrical transmission efficacy. While screening all these factors along side directionality performance was out of scope for this work, the

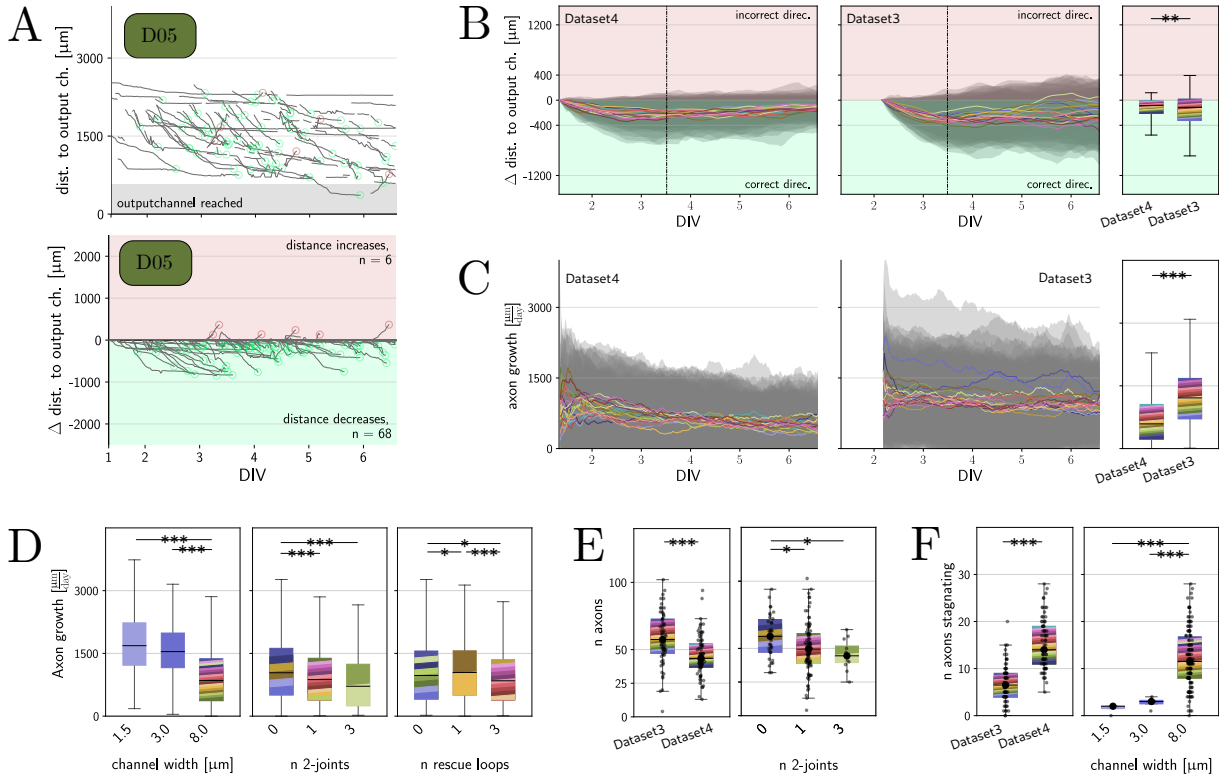


Figure 5: Between dataset variance and axonal viability. **A** Inferring directionality from distance-to-output channel exemplified in design 5. Each of the gray lines represents an axon identity, axons in the light gray region are inside the output channel. Subtracting the initial distance to the output channel yields the bottom plot. Green or red circles mark axons that grew at least 50 μm in the correct or incorrect direction, respectively. Count is given in corners. **B** Median growth directionality over time. Axon wise Δ directionality is computed by subtracting first- from last distance-to-output channel. Each colored line represents a design following the color code in Figure 4, gray regions indicate the standard deviation. **C** Axon growth velocity over time. **D** Axon growth velocity split by design feature. As for all following boxplots, whiskers represent 1.5 x inter quartile range (IQR), and colors represent the 21 designs composing the distribution according to the color code in Figure 4. **E** Number of axons identified in one half of a PDMS micro structure. Single dots represent datapoints composing the distribution. **F** Number of stagnating axons identified in one half of a PDMS micro structure. Kruskal-Wallis test was used for non-parametric group comparisons, subsequently, the single comparisons were made using Mann-Whitney-U test with Holm-Bonferroni correction. * indicates $p < 0.05$, ** $p < 0.005$, and *** $p < 0.0005$. Applies for subsequent figures.

tracking of growth cones yielded insights into frequency and velocity of axonal outgrowth. Intuitively, the frequency of outgrowth is directly derived from the number of unique axon identities. The growth velocity in [$\frac{\mu\text{m}}{\text{day}}$] was determined from the slope of distance-to-output channel over time (Figure 5 A). This allowed for a further metric, namely the classification of stagnating axons. Here, we defined axons as stagnating if the standard deviation of growth velocity over the last 5 h of detection was below 12 [$\frac{\mu\text{m}}{\text{day}}$]. In Figure 5 A (top) stagnating axons clearly appear as horizontal lines.

In accordance with the directionality discrepancy between datasets described above, the complementary metrics of outgrowth frequency, outgrowth velocity and stagnation frequency differ significantly between datasets (Figure 5 C,E,F). Figure 5 C illustrates

the growth speed over time for both datasets. Initially, the growth velocity is approximately 1100 [$\frac{\mu\text{m}}{\text{day}}$] with high variance. While the average growth velocity and variance decline over time in Dataset4, Dataset3 maintains the high initial outgrowth velocity. As expected, the number of stagnating axons per PDMS micro structure is significantly higher in Dataset4 (Figure 5 F). Lastly, the outgrowth frequency is significantly lower in Dataset4 (Figure 5 E).

So far, the data was only grouped by dataset. To reveal potential effects of different PDMS designs on the axonal viability metrics, the dataset may be split by design features, such as the channel width, the number of rescue loops, and the number of 2-joints. Figure 5 D shows the effect of these three features on axonal growth velocity. Especially the PDMS micro channel width has a highly significant effect. By almost completely eliminating stagnation (Figure 5 F), the Designs 03 and 04 which implement 3 and 1.5 μm wide channels respectively exhibit approximately double the growth velocity compared to 8 μm designs (see `D04_tracking.mp4`). A smaller yet highly significant relationship was identified between the number of 2-joints and rescue loops. Omitting both of these elements yields significantly higher growth velocity. While the number of 2-joints seems qualitatively anti correlated with growth velocity ($0 > 1 > 3$), the number of rescue loops is not, as designs with one rescue loop show significantly faster growth compared to designs with zero loops. Similar to growth velocity, the number of 2-joints seems to have a small negative effect on axonal outgrowth frequency (Figure 5 E).

5.5 Directionality in PDMS designs

Tracking growth cones provides insights into interesting axonal growth properties and their dependence on design features. However, the primary intention of tracking was to identify PDMS micro structure designs that result in high directional growth from seeding wells to output channel. As shown in Figure 5 A, the directionality is evaluated based on the A^* distance-to-output channel over time. A simple approach suitable for large effect sizes is to compare distributions of axon wise Δ distances (see Figure 5 B, right). This method favors long axon tracks, which is not of direct interest. Rather, the qualitative property of growing in the correct,- or incorrect direction is relevant (see circles in Figure 5 A). Figure 6 A summarizes those counts of axons for all 21 designs, normalized to the total number of observed axons. While none of the single comparisons pass statistical significance with Holm-Bonferroni correction, the factor *design* has a significant impact on backwards growth. Forward growth counts exceed backward growth across all designs since the initial outgrowth is strongly biased towards forward growth. With approximately 65 %, the highest median of forward growing axons is observed in design 4 implementing 1.5 μm wide channels. However, this strong forward bias comes at the cost of the relatively high backward growth of 25 %, which is also observed in design 3 using 3 μm wide channels. In contrast, design 8 implementing frequent, late merging shows nearly no backward growing axons paired with average forward growth. The Designs 12-20 which share the same general architecture but vary in specific motif designs collectively exhibit few (around 10 %) backwards growing axons. The forward growth distribution of design 18 using spiky tracts on unpreferred edges has the longest positive tail.

Grouping the data by design features instead of design can reveal more distinct trends. Figure 6 C and D summarize significant and non-significant effects, respectively. As men-

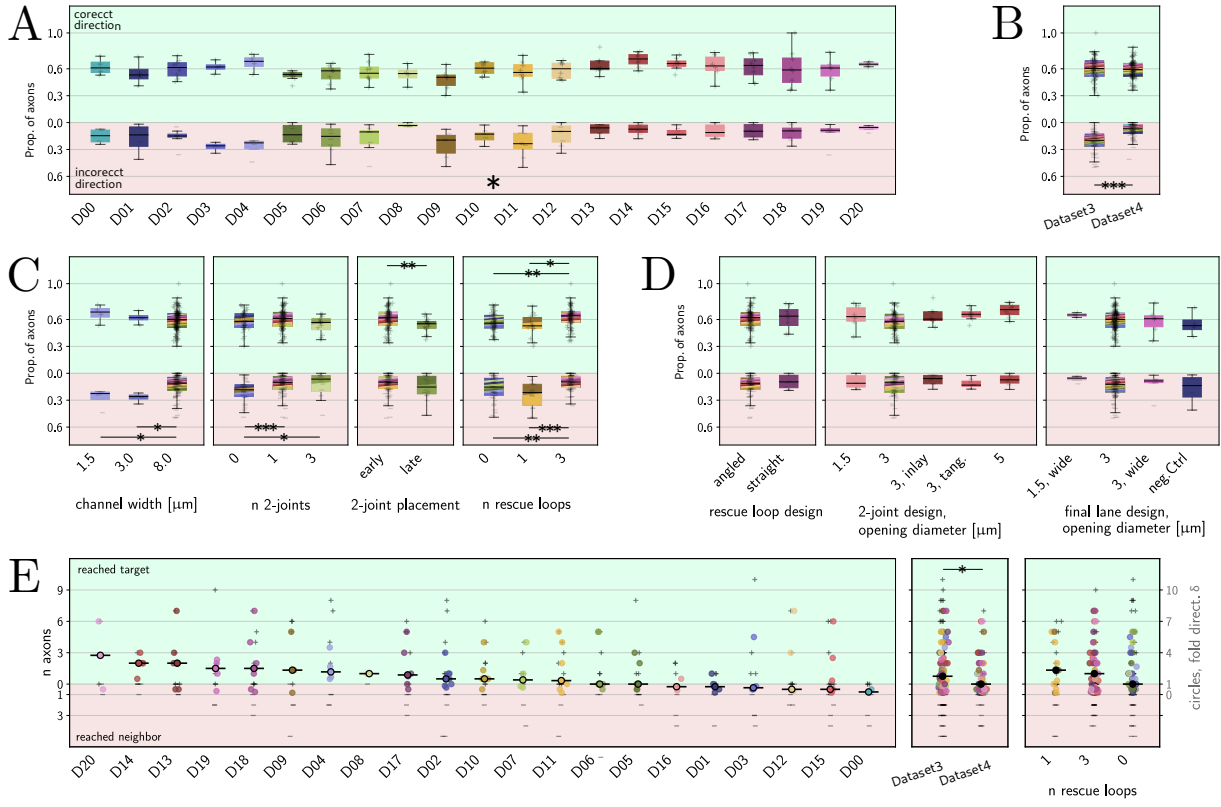


Figure 6: Directionality in PDMS designs. **A** Proportion of correctly,- and incorrectly growing axons in one half of a PDMS micro structure. Axons were counted if the Δ distance was above 50 μm . Faint + and - symbols compose the distributions, respectively. Applies for **B**, **C** and **D** as well. Star indicates that Kruskal-Wallis test evaluates the design as a significant factor for backwards growth, but single comparisons don't pass Mann-Whitney-U test with Holm-Bonferroni correction. **B** Number of correctly,- and incorrectly growing axons split by dataset. **C** Number of correctly,- and incorrectly growing axons split by significant features. **D** Number of correctly,- and incorrectly growing axons split by non-significant features. One other non-significant feature, the use of spiky tracts, is shown in Suppl. Figure 4 E. **E** PDMS micro structure designs ranked by δ fold directionality. Corresponding to the left y-axis labels, + and - symbols represent the number of axons that reached the output channel or neighbor, n_{target} , $n_{\text{neighbour}}$, respectively. The colored circles represent the smoothed δ fold directionality computed from these two counts as formulated in equation 4, medians are indicated by horizontal lines. The axis labelling on the right applies for all circles.

tioned before, smaller channel widths increase both forward,- and backward bias, however, only the backward effect is statistically significant. Another significant design feature is the number of 2-joints, or merging structures. Using one or three instead of none yields significantly lower backwards growth, whilst not affecting the forward bias. Conversely, forward bias is significantly impacted by the placement of 2-joints but does not have an effect on backwards growth counts. Joining channels early yields a significant increase in forward growth of approximately 10 %. Lastly, the number of rescue loops has an impact on both forward,- and backwards growth. Implementing three instead of one or none rescue loops prior to each 2-joint reduces the proportion of backwards growing axons. Forward bias was significantly increased between three and fewer than three rescue loops. No significant effects were observed for angled versus straight rescue loop designs, spiky tracts, different variants of 2-joints and modifications to the final lane design (Figure 6 D).

As mentioned in the methods (4.2.6), focusing solely on growth direction counts may overestimate the performance of designs with low to medium forward convergence that do not reach critical joining areas. This is observed when splitting by dataset origin, as shown in Figure 6 B. Timelapse videos of Dataset4 show only few axons reaching 2-joints or final lane, thus backwards growth is significantly biased towards lower values. To compute an interpretable directionality metric that mitigates this directionality overestimation, we compute the ratio of axons reaching the output channel and axons reaching neighbors. Ranked by performance, both single axon counts and δ fold directionality are shown in Figure 6 E. Due to many samples showing neither target,- nor neighbor grown axons, δ measures were limited to fewer samples, resulting in almost no significant differences. Still, the metric provides valuable qualitative insights in comparison to directional counts in Figure 6 A. Consistent with good performance on growth direction counts, the five Designs 20, 14, 13, 19, and 18 show δ fold directionality between almost 4 and 2.5 (see D20_tracking.mp4). Hinting at the potential discrepancy between the two metrics, design 9 δ performance shows a tendency to be better than what relative growth direction counts indicate. δ below 1 is observed in Design 00 (see D00_tracking.mp4), 15, 12, 03, 01, and 16. These designs implementing no final lane, a final lane with,- and without directional promoting geometry, and 2-joints with medium-sized and tangent entries exhibit more axons reaching the neighbor than the output channel. The only significant differences in δ are observed when grouping by dataset. In sharp contrast to results in Figure 6 B, design measurements originating from Dataset4 show lower performance than those from Dataset3, highlighting the overestimation bias of counted growth direction clearly. In line with the observation in Figure 6 C, though not significant, the implementation of rescue loops tends to have a positive effect on the δ metric (Figure 6 E, right).

5.6 Axon guidance design primitives

By tracking axons through PDMS channels during the initial growth phase, we identified micro structure designs with notable directionality. While number,- and placement of 2 joints, channel width and number of rescue loops had a significant impact on directionality performance, more settle and specific design motif alterations introduced to the final lane and 2-joints did not elicit significant differences. To identify PDMS motif designs that impact directional growth, we designed PDMS micro structures that answer specific questions about both chemical and structural axon guidance. The experimental setups and results of testing these guidance primitives are presented in Figure 7.

Chemical guidance was investigated by creating a differential attractor cue concentration at a growth decision point (Figure 7 A). The aim was to create a chemical gradient by introducing differential channel lengths towards a seeding well containing a thalamus spheroid. We do not observe biased growth along the shortest path towards an attractor, not even if the ratio between the two channel lengths is as high as six.

PDMS geometry based axon guidance relies on the tendency of axons to adhere to edges and avoid sharp turns. In scenarios such as channel merging, final lane merging, and rescue loops, we aim to direct axon growth towards a preferred edge that guides towards the preferred direction. Figure 7 B shows the results of comparing edge transition motifs parameterized by two factors, the radius r guiding towards the preferred

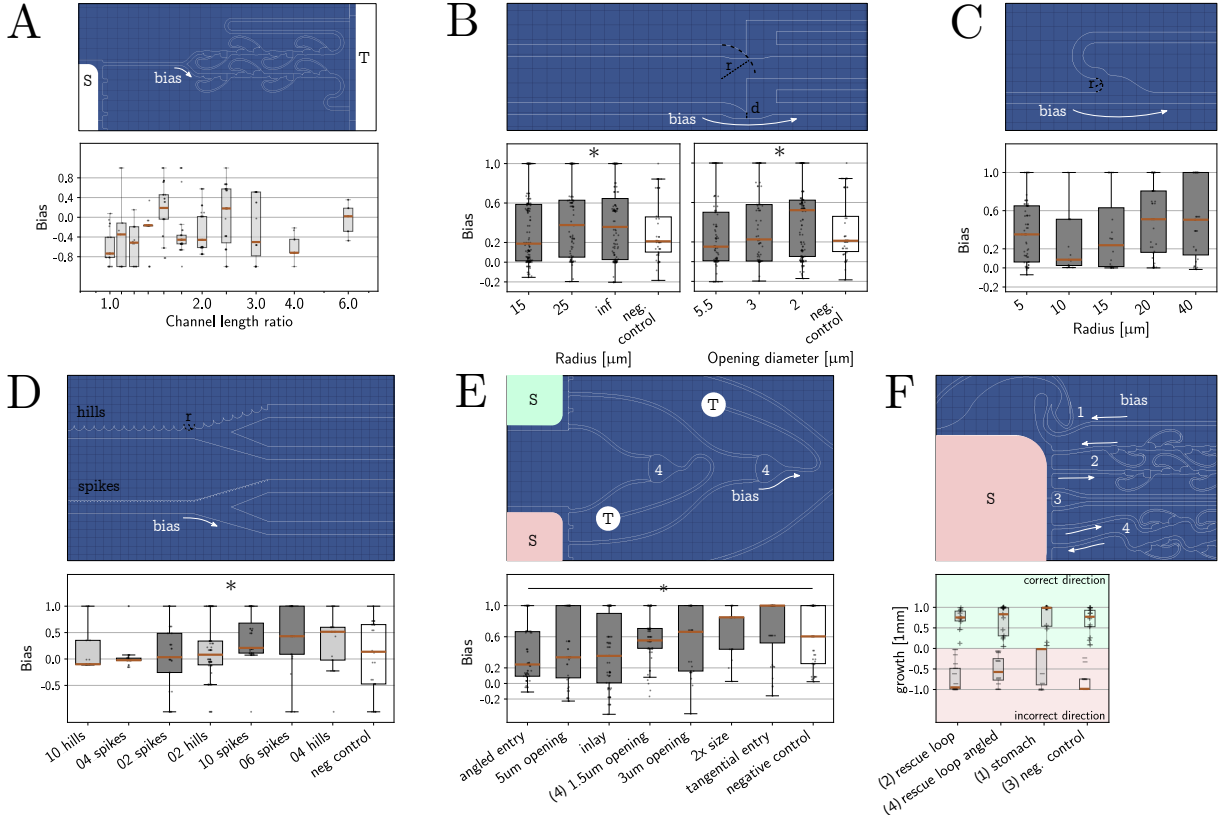


Figure 7: Axon guidance primitives in micro structure designs. All PDMS micro structure designs show RGC left-to-right growth from seeding well (S) to target well (T). **A** Effect of cue gradient on directional growth introduced by varying attractor channel length from seeding well (S) towards the thalamic cue source (T). A ratio of 6 translates into channels with a length 480 μm , and 6 x 480 μm . **B** Edge transition motif parameters radius r and opening diameter d . The negative control omits the edge transition feature. Infinite r refers to designs where the input channel is tilted up by 45° . **C** Radial detachment for varying radii r . **D** Introduction of edge-detaching features. Light gray bars used hills, dark gray indicates the use of spikes instead. **E** 2-joint or merging structure design. Source wells (S) are seeded with GFP, and RFP labelled RGCs, respectively. Here, the bias metric β replaces I_{bias} with I_{inlet} in equation 5. The shown 2-joint design is number 4, using an opening diameter 1.5 μm . **F** Directionality constraint growth. Similar to E but here connected with asymmetric channels, two opposing wells are seeded with GFP- (not shown) and RFP labelled RGCs. Four different design motifs are compared in terms of maximum distance reached. Red lines indicate median forward-, (green) and backward (red) distance reached. As in previous figures, stars without lines indicate Kruskal-Wallis test evaluating to $p < 0.05$, lines translate into subsequent Mann-Whitney-U tests also outputting $p < 0.05$.

edge, and the opening diameter d between edges. Both factors significantly bias growth direction, however, no single comparisons pass significance with Holm-Bonferroni correction. Qualitatively, it seems that larger radii guiding towards the preferred edge improve edge transitions, but returns diminish for very large radii. Also, successful edge transition seems to occur more frequently when the opening diameter is 2 μm instead of 5.5 or 3. Both 5.5 and 3 μm openings show little growth bias difference with the control, indicating the importance of small diameters. In Figure 6 C, we aimed to test axon detachment behavior when growing along differentially sharp radii. Although previously published stomach structures seem to rely on this principle (Forró et al. 2018), we do not

find a significant relationship between small radii supposedly inducing an edge transition, and a directional growth bias. The previous two primitives investigated the process of edge transitioning at joining or rescuing motifs, however, one may also consider channel designs that promote growth on preferred edges a priori. Figure 7 D shows experiments implementing hill,- and spike-like edge features of varying radius to drive axon growth on the opposing edge. Again, while this factor passes significance, single comparisons do not. It seems however, as if both hills and spikes of medium radius (4, and 6 μm) are able to bias growth in one direction.

The primitives investigated in Figure 6 A-D aimed to find optimal low-level building blocks for designing axon-guiding micro structures. In Figure 7 E and F, we reduce the abstraction level in testing practical PDMS micro structure motifs to merge channels and achieve directional growth. 8 different 2-joint designs were tested in terms of their ability to merge two channels with minimal cross growth (Figure 7 E). Due to the control performing surprisingly well, the only 2-joint significantly differing from control after multiple testing correction was design 1 using angled joint entries. The highest median growth bias was observed in 2-joints using tangential edge transitions. Lastly, we tested the ability of three different designs to achieve directional growth from one node to another (Figure 7 F). Although again not statistically significant, previously published stomach structures show very low median backwards growth. Angled rescue loops seem to perform slightly better than non-angled ones in preventing backwards growth. Forward growth is not negatively affected in any of the designs.

6 Discussion

6.1 Summary

This work set out to identify PDMS micro structures that directionally connect multiple source nodes with a common target. Solving this problem would not only be highly beneficial for biohybrid brain interfacing technology as described in the introduction, but also for functionally more sophisticated neural network models. To screen the 21 previously designed PDMS micro structures at high throughput, we resorted to a computationally aided anatomical readout. Our deep-learning based growth cone tracking model is able to accurately detect growth cones of various morphologies and successfully link them to long living axon identities. The obtained axon tracks allowed us to derive information on the degree of directional growth, growth velocity and the number of outgrowing axons. By virtue of the systematically parameterized 21 designs, we were further able to identify trends between these metrics and specific design features.

Compared to 8 μm wide channels, we find that narrow channel widths such as 1.5 and 3 μm eliminate axon stagnation and significantly increase axonal growth velocity by almost two folds. Conversely, introducing more sophisticated design motifs such as 2-joints or rescue loops reduced growth velocity, with the number of 2-joints additionally reducing the frequency of axonal outgrowth. When comparing the relative proportion of backwards growing axons across the 21 designs, we find a significant relationship, but forward growth does not differ significantly. Various features such as channel width, the number of 2-joints and the number of rescue loops significantly affect backwards directionality. Forward growth differs in designs varying in 2-joint placement and number of

rescue loops. Next, to find the best performing design and assign an interpretable directionality metric, we calculated a ratio of target-grown and cross-grown axons. With a fold directionality between almost 4 and 2.5, this metric identified Design 20, 14, 13, 19 and 18 implementing one 2-joint, three rescue loops and altered final lanes and 2-joints as the best performing ones.

While the tracking of growth cones through PDMS micro structures revealed highly directional designs, the experimental resolution was insufficient to disentangle more settle factors such as specific 2-joint motif designs. For this reason, we designed new PDMS micro structures that systematically investigate axon guidance primitives. Due to many group variants, low sample sizes, and high variance, single comparisons were rarely significant after multiple testing correction. Still, these experiments revealed interesting trends that enabled us to make predictions about successful followup designs. The following discusses the above in more detail.

6.2 Growth cone tracking

The implemented growth cone tracking model follows the common approach of splitting the tracking problem into instance detection and identity association. On test data, the model achieves detection F1 scores of 0.76. Subsequent identity association reduces performances marginally by 0.05 to 0.71. Intuitively speaking, 7 out of 10 growth cone identifications will be correct, 3 will either be false positives, false negatives or wrongly associated.

The tracker shows good generalization from train,- to test datasets, however, meaningful model performance evaluation needs to incorporate generalization from test,- to inference data as well. To expose the model to various growth cone location contexts, the model was trained on three different PDMS micro structure designs. This showed vastly improved generalization versus training on datasets with a single PDMS micro structure design. Based on extensive qualitative checking, with minor exceptions, we can report a solid overall generalization ability to various PDMS micro structure designs. These exceptions include out-of-focus timelapse recordings, and, limited to one experiment, detection of growth cones in 1.5, and 3 μm wide channels. We also observe that growth cones are tracked less well in structures that are rarely present in the training data, including rescue loops and the output channel. As commonly observed in deep learning models (Azulay and Weiss 2018), the method is highly sensitive to deviating pixel intensity distributions. For new datasets, it is therefore essential to carefully replicate the confocal image acquisition settings.

Not many solutions exist for the specific problem of growth cone tracking. Relying on classical computer vision tools, Keenan et al. 2006 presented a method that requires human assistance and clearly separated axons for successful growth cone tracking. This early method did not fullfil our requirements in terms of experimental throughput. An indirect approach inferring axonal growth patterns from segmented and associated video frames also showed results restricted to predominantly well separated axons (Liu, Cootes, and Ballestrem 2020). Compared to a classical *in vitro* setup, segmenting single axons in densely packed PDMS micro channels is additionally challenging, since axons show heavy overlap. Also, Liu, Cootes, and Ballestrem 2020 did not publish an implementation for

open-source use. Another alternative relying on segmentation based tracking are commercial solutions such as Incucyte by Sartorius, but they likely suffer from the same problem. Classical non-machine learning based particle tracking tools bundled in the Imaris imaging software (Oxford Instruments) did not perform comparable to our method either. Another view on tracking growth cones in timelapse image sequences is to treat the temporal dimension as a spatial one. Targeting mainly connectomics, extensive work exists on axon segmentation in 3D microscopy slices (Funke et al. 2019, Abdollahzadeh et al. 2021), however the z-dimension in these datasets does not comprehensively translate to the temporal dimension in video tracking. The specific objects of interest, growth cones, are rarely present in 3D microscopy slices. For the reasons mentioned above, benchmarking our method is not straight forward. Since, to our knowledge, no MOTA performance scores have been reported on growth cone tracking, we looked into the reported MOTA scores on the cell tracking with mitosis detection (CTMC) dataset (Anjum and Gurari 2020). Here, state of the art performance reaches MOTA scores of 0.5, whereas our tracker has a MOTA of 0.61. Of course, this may be due to the CTMC dataset being far more challenging, but still, this crude comparison indicates at least decent performance of our tracker.

A collection of model modifications could be made to potentially improve tracking performance. First, the implemented YOLO detector would likely be outperformed by the well established Faster R-CNN architecture (Ren et al. 2015 and Introduction). The YOLO detector was implemented because of its wide adoption, but the advantage of fast online detection is not a relevant feature in our offline detection use case. The model performance would also likely increase with more training data including morphological growth cone outliers and less common PDMS design motifs. Lastly, for long timelapse recordings, the PyTorch based video leading needs to be reimplemented as currently, the entire image sequence is put in system memory.

6.3 Directional PDMS micro structures

The degree of directional growth through PDMS micro structures was screened by growth cone tracking in 21 many-to-one designs, and by performing axon growth experiments investigating lower level guidance primitives. While the tracking in multiple-source to single-target PDMS micro structures aimed to find the best performing design, the investigation of axon guidance primitives took a conceptual step back, answering specific design optimization questions.

6.3.1 Micro channel width

Besides information on directional growth, tracking provided insights into axon growth velocity and outgrowth frequency, revealing a strong relationship between channel width and axon growth velocity. By reducing the channel width from 8 to 3 or 1.5 μm , we observe an increase in median growth velocity from 750 to 1600 μm per day (DIV 3.5-6.5). For aggregated cortical neurons grown in agarose microcolumns, Adewole et al. 2021 presented similar growth velocities peaking at DIV 3. Classifying stagnating axons in PDMS micro structures revealed that designs utilizing narrow channels showed significantly fewer stagnating axons than wide-channel counter parts. Based on the observation that growth stagnation mostly occurs during the first 200 μm , one hypothesis could be that dentritic

structures selectively enter and cloak channels wider than 3 μm .

These high velocities do not necessarily lead to the conclusion, that the majority of axons will cover distances of 3 mm in 2-4 days. First, it should be considered the growth velocity is likely to drop over time as shown in Adewole et al. 2021. Second, fast, short living axon identities may achieve growth velocities beyond 2 mm per day, yet only cover a few hundred μm . On top of that, similar to the discrepancy between 8 and 1.5 μm channels, growth velocity declines when axons enter the 75 x 75 μm output channel. For these reasons, we only see RGCs reaching the 3-4 mm distant target after approximately 12 days (see Figure 1).

Through the strong forward convergence, Design 3 implementing 3 μm wide channels achieved δ fold directionality above one, indicating a positive effect of smaller channels on directionality. While these narrow channel designs could be highly interesting for guidance motifs relying on high growth velocities, the long time neural viability and signal transmission efficacy would first need to be validated.

6.3.2 Merging channels

Any design that aims to guide multiple source nodes towards a common target node inevitably needs to merge channels. Crucially, these merging elements also present the opportunity for axons to cross-grow towards a neighboring node. Thus, achieving directional merging is the central problem to solve for engineering directional many-to-one PDMS micro structures.

Our 21 designs broadly implement three approaches to merging: (i) merging channels using 2-joints, (ii) merging channels in a final lane, and the outlier approach (iii), collecting axons in a large container. Design 00 solely follows approach (iii), Designs 01-04 rely only on (ii) and the Designs 05-20 implement both (i) and (ii). An illustration of 2-joints and final lanes is shown in Figure 4.

Guiding channels in an axon collection container with a diode-like geometry (iii) does not yield high directionality, as seen in Design 00. Due to missing edges, axons entering the container compartment slow down significantly and frequently enter neighboring nodes regardless of the diode-like entry geometry (see D00_tracking.mp4).

In contrast, the addition of 2-joints significantly reduces the degree of backwards growth in PDMS designs, albeit that no significant difference is observed between the use of one or three 2-joints. Additionally, placing them early, and thus closer to source nodes yields significantly higher forward growth. This positive effect may be due to neighboring nodes emitting growth promoting chemical cues. While the addition of at least one 2-joints significantly reduces backwards growth, it seems to negatively affect the frequency and velocity of axonal outgrowth. Designs omitting 2-joints exhibit a median number of 65 axons per micro structure half, while designs with one or three 2-joints, showed only 50 and 40 axons, respectively. This may be caused by a thalamic cue diffusion bottleneck introduced by joining lanes together. The growth velocity may be reduced due to deceased edge attachment within 2-joints.

As mentioned above, we do not observe a significant directionality difference between designs implementing one or three 2-joints. However, assuming that final lane merging (ii) does not outperform 2-joint merging (i) by a large degree, there exists a theoretical advantage of using 2-joints over final lane joints, especially when scaling up the number of source nodes. As a function of the number of source nodes x , consider the integer $n(x)$

referring to the number of directional axon transitions needed to obtain a completely directional culture. For example, following approach (i), four source nodes merged with three stacked 2-joints evaluate to $n_{(i)}(4) = 2 + 2 + 2 + 2 = 8$, since each source channel passes two growth decision points. Interestingly, for an increasing number of source nodes x , designs joining through final lanes require vastly more favorable axon transitions $n_{(ii)}$ than designs relying on 2-joints $n_{(i)}$ (see equation 8, 9, and $x = 32$). Final lanes may still be competitive if merging directionality is vastly higher than in 2-joints, however, since we do not observe exceptional directionality in designs relying solely on final lane merging, we may assume that 2-joints merge at least as directional as final lanes. Final lane joining seems to positively impact axonal outgrowth frequency and velocity, but for maximally directional cultures integrating many source nodes, stacked 2-joints are likely preferred. The Designs 06 and 08 integrating three stacked 2-joints did perhaps not outperform one 2-joint counter parts, because they did not integrate rescue loops.

$$\begin{array}{cccc} \hline x & 8 & 16 & 32 \\ \hline n_{(i)}(x) & 24 & 64 & 160 \\ n_{(ii)}(x) & 35 & 135 & 527 \end{array} \quad n_{(i)}(x) = x \log_2 x \quad (8)$$

$$n_{(ii)}(x) = x - 1 + \sum_{j=1}^{x-1} j \approx \frac{1}{2}x^2 \quad (9)$$

An intuitive next step for improving directional merging was to investigate optimal 2-joint merging designs. Since directionality performance of Designs 12-15 did not differ significantly, we designed a PDMS micro structure specifically testing various 2-joint designs. Although the Kruskal-Wallis test identified the 2-joint designs as originating from different distributions, only a design implementing angled joint entries significantly underperformed versus the control. The control joint showed a median merging bias β of 0.6, whereas we expect β to be 0 for non-directional 2-joint designs. This surprisingly high performance raised the bar for reaching significance. The non-significant trends of merging performance we see in these primitive experiments and the Designs 12-15 do not coincide. Wheres tangential joint entries, doubling the 2-joint size, and 3 μm joint entries perform well in the isolated 2-joint screen, Designs 13 and 14 using 2-joints with inlays and 5 μm entries respectively tended to be more directional in tracking experiments. One issue reducing the experimental resolution of the primitive screen was that successfully merged axons occasionally turned 180 degrees within the diffusion well, and grew backwards into the 2-joint, therefore confounding the measured directionality. To avoid this and find significant differences, more replicates are required at a preferably early timepoint such as DIV 7.

6.3.3 Grwoth direction rescue loops

The evaluation of $n_{(i)}(x)$ for 32 source nodes aptly highlights the difficulty of engineering directional many-to-one PDMS micro structures (equation 8). Even when merging with 99% directionality, the joint event of entirely correct transitions within a culture occurs only with a probability of $0.99^{160} = 0.2$. One approach to alleviate the impact of merging is to introduce rescue structures that selectively redirect wrongly growing axons. Thereby, transitions within a 2-joint can be mitigated by preventing axons from reaching neighboring nodes. As mentioned in the introduction, a multitude of PDMS geometries have been published to impose growth directionality. Stomach structures showed direc-

tionality of up to 95% for connecting two nodes (Forró et al. 2018), however their design is not directly transferable to multiple source nodes converging on a common target. For this reason, we designed new growth-rescuing loop structures that are small and easily stackable. Importantly, the forward growth is not impaired, but even increased in designs implementing three instead of one or zero rescue loops. Although we observe lower axonal growth velocity when three of these rescue loops are added prior to merging, the relative number of backwards growing axons is significantly reduced. One caveat to this is that, although not statistically significant, one rescue loop designs seem to be less directional and promote faster growth than zero rescue loop designs. Analyzing the feature of *n rescue loops* as a numerical,- instead of categorical variable may result in a different conclusion.

To investigate settle design variations between rescue loops, and to compare them to previously published stomach structures, we performed an additional experiment specifically targeting directional growth. The setup consisted of two GFP, and RFP labelled nodes connected through channels with,- and without directionality imposing motifs. Similar to 2-joint comparisons, the results were impaired by many axons growing a loop from the target back to the source node, using the non-directional control channels. Discerning if a GFP labelled axons originated from the source or target node was thus often not possible. To prevent an over,- and underestimation of forward and backwards growth respectively, a second iteration of this experiment should only test a single design between two nodes.

Though not significant, we see that stomachs successfully prevent backwards growth, angled rescue loops tend to be more directional than straight ones, and forward growth is unimpaired across the board. Between Design 12 using angled rescue loops and Design 16 using straight ones, no significant difference is observed.

6.3.4 Bias of between dataset variance

One of the most dominant trends in the axon tracking data was found between Datasets 3 and 4, which originated from two independently conducted experiments. Dataset 4 showed significantly less frequent axonal outgrowth, lower growth velocity, and more stagnating axons. On top of this, due to the majority of axons not reaching critical merging regions, the directionality performance differed only marginally between designs. This resulted in an overestimation of directionality scores when only the growth direction was evaluated. To address this bias, we additionally looked into the fold directionality defined as the ratio of target,- and neighbor reaching axons. Here, samples from Dataset 4 showed significantly lower performance than those of Dataset 3.

This discrepancy needs to be discussed because a subset of designs were only included in one of the two datasets. Designs 03 and 04 using narrower channels were dropped from Dataset 4 due to poor tracking accuracy. Importantly, the relationship between narrow channels and increased growth velocity was qualitatively observed in Dataset 4 as well. Designs present only in Dataset 4 included 00, 08, and 20. For these designs, the dataset-wide bias on for example growth velocity and directionality needs to be carefully considered when interpreting the results. The negative negative relationship between number of 2-joints and growth velocity is one such example. This trend might be biased since one of the two three 2-joint designs, Design 08, carries the low growth velocity bias present in Dataset 4.

A multitude of factors might have caused diminished axonal viability in Dataset 4. PDL or Laminin coatings may have been of inferior quality, the retinal tissue might have stayed in Hibernate medium for too long, or problems during dissociation could have harmed the RGCs. Another hypothesis is that the slightly differing experimental setups between the two experiments caused the significant deviations. While Dataset 3 used free floating thalamic tissue pieces enclosed by a PDMS frame for chemical attraction, in Dataset 4, 3 mm distant stomach target structures were seeded with a thalamus spheroid. This may have resulted in significantly lower attractor cue concentration.

6.3.5 Axon guidance primitives

Both merging and rescue loop motif designs are based on axon growth bias towards edge attachment and the avoidance of sharp turning. However the details of these growth biases are poorly characterized. To find elucidate these primitives of axon guidance, we performed a range of experiments. Addressing chemical guidance, we designed PDMS micro structures integrating growth decisions points with varying channel distances towards a chemical attractor. Even when one channel was 6x longer than the other, we did find biased growth into the shorter channel. It is conceivable that too little thalamic attractor entered channels in general, creating negligible cue gradients at the decision point. Also, the experimental setup may be flawed because, at chemical equilibrium, the growth decision region may not exhibit a differential attractor cue gradient between the two channels. Since the cultures were imaged at DIV 7 and 14, the chemical gradient may have been insufficient. To avoid the necessity of axons reaching growth decision points before chemical equilibrium, a new experiment could investigate the growth bias between different tissues. Such a micro structure would more closely resemble final lane joints where thalamic attractor concentration is expected to be higher than competing cues emitted by neighboring RGC source nodes.

Besides experiments on chemical guidance, we tested the impact of specific PDMS geometries on mechanical axon guidance, specifically on edge attachment and edge transitioning. For concave edge transition motifs, both the radius r and opening diameter d were identified as significant factors for guiding axons from one edge to another. We see a non-significant trend indicating the benefit of large radii and small opening diameters of $2 \mu\text{m}$. While 2-joints integrating $1.5 \mu\text{m}$ wide entries did not achieve particularly high directionality, small entries into a wide final lane as used by Design 20 resulted in the highest fold directionality out of all designs (see `D20_tracking.mp4`).

Instead of integrating concave detachment from an unpreferred edge, we also considered convex or radial detachment utilized i.a. in stomach structures. Surprisingly, we don't find a relation between small radii and an edge detachment bias promoting directional growth. Considering that only few axons reached the decision area in these micro structures, the results may be due to an insufficient sample size.

Lastly, we considered biasing the growth on the preferred edge *a priori* by adding spike-, or hill like features to the unpreferred edge. This was found to be a significant factor effecting the growth bias at a decision point. However, again, single comparisons against the control with Holm-Bonferroni correction were not significant. Using hill-like features with a radius of $4 \mu\text{m}$, or spike features with a radius of $6 \mu\text{m}$ showed a tendency towards biasing axonal growth. Design 18 implementing spiky tracks did not perform significantly better than designs omitting spikes. This result is in accordance with the primitive experiment, since Design 18 implemented spikes of radius $2\text{-}3 \mu\text{m}$. These features did likely

did not resolve during micro fabrication, and therefore failed to bias growth direction.

6.4 Conclusion & Outlook

In this work, we screened 21 many-to-one PDMS micro structure designs for directional growth towards an output channel. To do this at high-throughput, we build a machine learning based growth cone tracking model enabling us to identify correctly,- and incorrectly growing axons. The best performing design exhibited a median fold directionality of almost 4, which translates into this design exhibiting 4 times as many axons in the output channel, as in neighboring RGC wells. To further optimize design primitives such as merging structures and rescue loops, we designed followup experiments investigating axon guidance at a lower abstraction level. While these experiments did not reveal clearly optimal 2-joint designs, they indicated the advantage of spikes on unpreferred edges and small between-edge distances when transitioning to preferred edges.

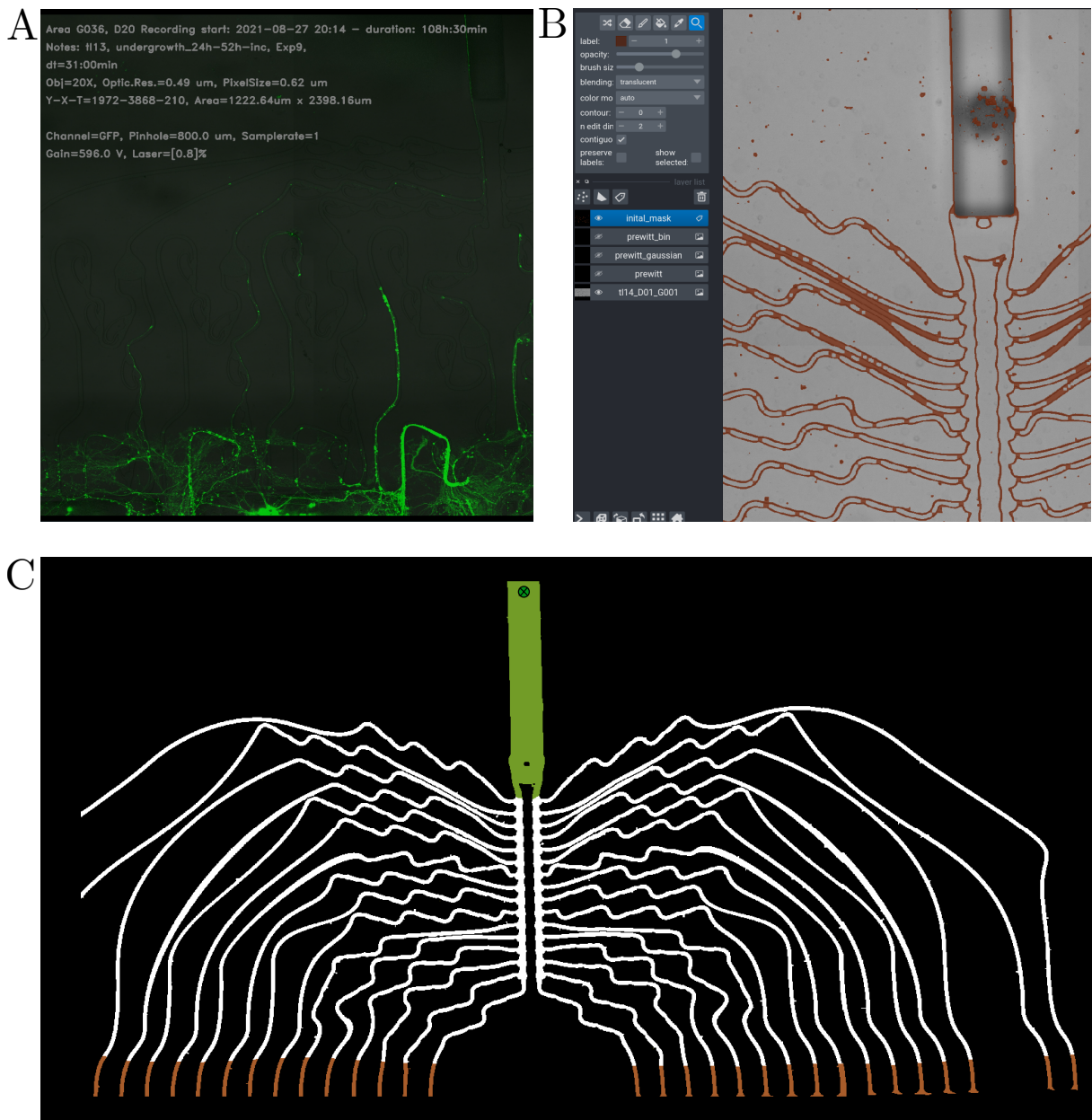
Using Design 20 showing a directionality bias of nearly 4 fold, ensuing iterations of biohybrid neural implants will benefit from fast convergence towards the final lane while cross growth to neighboring seeding wells is minimized.

A crucially important followup to this work is the functional confirmation of directional connectivity within PDMS micro structure designs. While anatomical directionality screens have the advantage of high throughput, the final metric of interest is the number of functionally independent electrical channels driving activity in the target tissue. Since all of the 21 micro structures were designed to fit electrode patterns on glass multi electrode arrays (glass MEAs), this data can be acquired without difficulty.

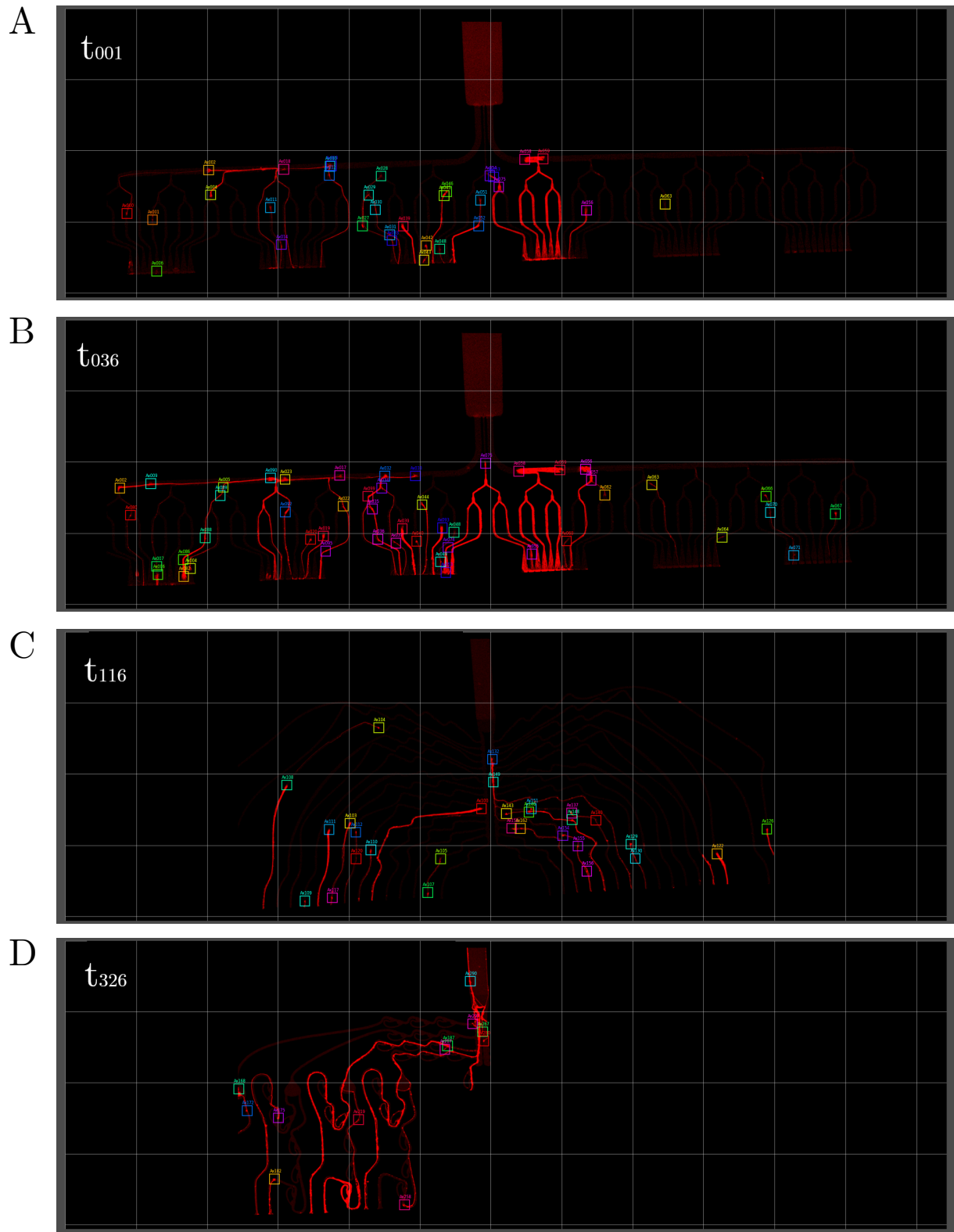
Although a subset of the 21 designs showed already impressive directionality, there is likely room for further improvement. Future designs should integrate narrow channels for higher growth velocities and potential benefits on channel merging. Primitive experiments testing the performance of 2-joints should be repeated to identify significant performance differences. Using optimal 2-joints, new designs should try to integrate as many angled rescue loops as possible. Further, the potential advantage of using closely positioned thalamic tissue pieces as chemical attractors should be investigated more rigorously.

Lastly, another interesting avenue of future research could be a super-high-resolution screen of axonal growth behavior, using the growth cone tracking model. This could reveal exact dynamics of edge transitioning and attachment, growth cone stagnation and collapse, and turning,- retraction and exploration behavior. From this low level knowledge, we could design PDMS micro structures specifically tailored to growth cone dynamics. Growth cone tracking at scale could also be used for studying branching behavior and target tissue innervation.

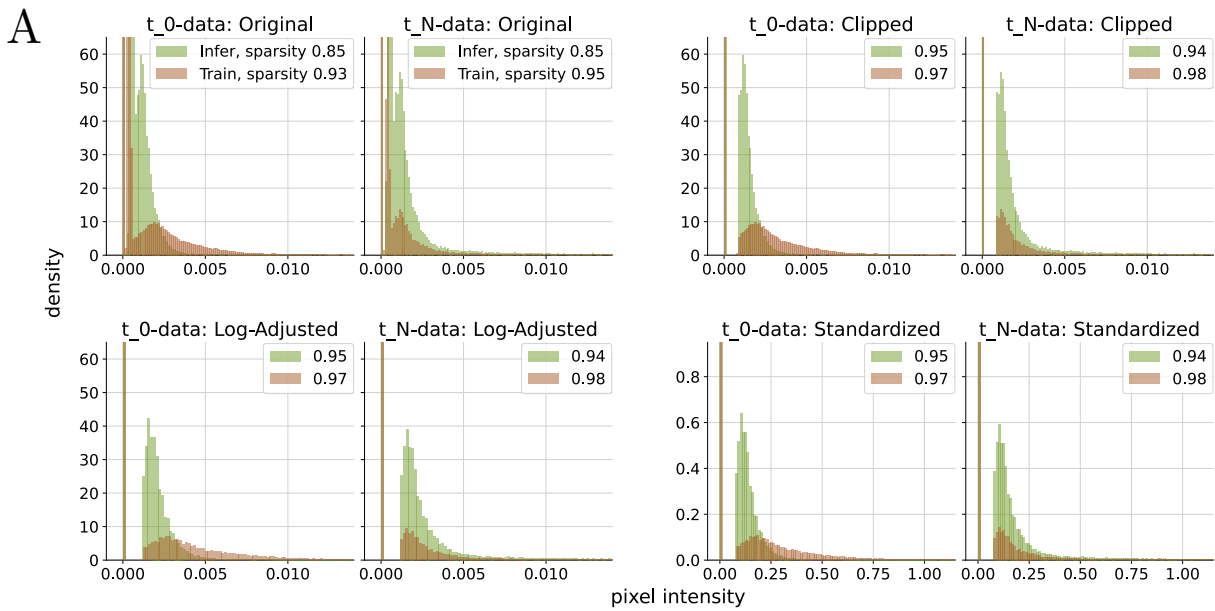
7 Supplementary Figures



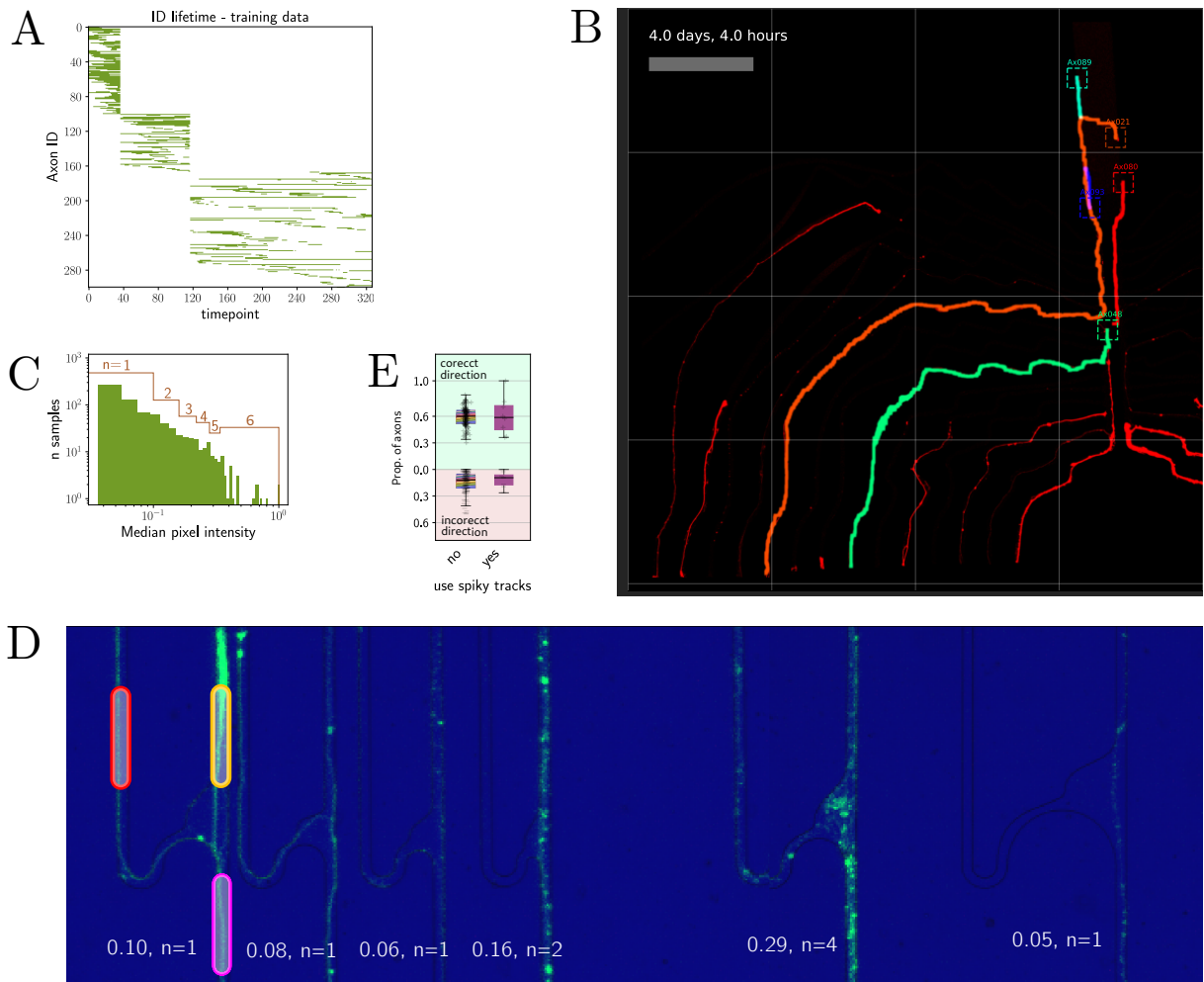
Supplementary Figure 1: Initial timelapse preprocessing steps. **A** A snapshot of the exported video including the relevant metadata of the recording. **B** The napari image viewer interface with the edge segmentation layer in brown. **C** The manually segmented binary mask of the micro channels in non-black, the output channel in green, and the exiting channels in brown. The green dot in the output channel marks the target point of the PDMS design.



Supplementary Figure 2: Labelled training data examples. **A** shows the first frame of the training data sequence. Each box represents a growth cone, the color indicates the identity over consecutive frames. **B** shows the last frame of Dataset1. **C** shows the last frame of Dataset2, PDMS micro structure 1 (compare Table 2). **D** shows the last frame of Dataset2, PDMS micro structure 2. Gridsize = 317 μm .



Supplementary Figure 3: Preprocessing effects on pixel intensity distributions. **A** Pixel intensity distribution of training-, and inference data at t_0 and t_N over three major preprocessing steps. The two plots top left show the initial pixel intensity distributions, top right after clipping, bottom left after log adjusting, and bottom right after standardization. Histograms on the left were obtained from sampling 10^6 pixel values from the first frame, histograms on the right from the last respective frame. The inference data to produce the histograms (brown) was taken from a representative image sequence from Dataset3 (see Table 2). The number in the legend indicates the proportion of image values equal to zero (sparsity). Note that outlier intensity values are not shown.



Supplementary Figure 4: Methodology illustrations. **A** illustrates the axon identify lifetime. A green point on this pixel map indicates that a label exists for the matching axon identity and frame. The three clusters originate from the concatenation of three PDMS micro structure timelapse videos. **B** Axon reconstruction from growth cone track. For clarity, only a subset of identified axons is drawn. Gray bar width is 200 μm . **C** Estimation of n axons/ duplicates (brown) from median intensities (green) for primitives analysis. Note double log scales. **D** Design primitives analysis example. Shown is the intermediate analysis output for the radial detachment primitive. The pink, yellow, and red boxes indicate the regions for computing inlet, biased, and unbiased median intensity, respectively. Annotated numbers refer to inlet median intensity and the resulting number of duplicates n . **E** Proportion of axons growing in the correct,- and incorrect direction, respectively. Split by using spiky tracks or not. This extends the panel from Figure 6 D summarizing tje design features not significantly effecting directionality. Moved for visual clarity.

References

- Mead, Carver (1989). *Analog VLSI Implementation of Neural Systems*. Ed. by Carver Mead and Mohammed Ismail. Vol. 80. Springer US. ISBN: 978-1-4612-8905-0. DOI: 10.1007/978-1-4613-1639-8. URL: <http://link.springer.com/10.1007/978-1-4613-1639-8>.
- Durand, Dominique M. (Sept. 2006). "What is Neural Engineering?" In: *Journal of Neural Engineering* 4 (4), E01. ISSN: 1741-2552. DOI: 10.1088/1741-2552/4/4/E01. URL: <https://iopscience.iop.org/article/10.1088/1741-2552/4/4/E01> <https://iopscience.iop.org/article/10.1088/1741-2552/4/4/E01/meta>.
- Maynard, Edwin M., Craig T. Nordhausen, and Richard A. Normann (1997). "The Utah intracortical Electrode Array: a recording structure for potential brain-computer interfaces". In: *Electroencephalography and clinical neurophysiology* 102 (3), pp. 228–239. ISSN: 0013-4694. DOI: 10.1016/S0013-4694(96)95176-0. URL: <https://pubmed.ncbi.nlm.nih.gov/9129578/>.
- Jun, James J. et al. (Nov. 2017). "Fully integrated silicon probes for high-density recording of neural activity". In: *Nature* 2017 551:7679 551 (7679), pp. 232–236. ISSN: 1476-4687. DOI: 10.1038/nature24636. URL: <https://www.nature.com/articles/nature24636>.
- Stevenson, Ian H. and Konrad P. Kording (Jan. 2011). "How advances in neural recording affect data analysis". In: *Nature Neuroscience* 2011 14:2 14 (2), pp. 139–142. ISSN: 1546-1726. DOI: 10.1038/nn.2731. URL: <https://www.nature.com/articles/nn.2731>.
- Herrington, Todd M., Jennifer J. Cheng, and Emad N. Eskandar (Jan. 2016). "Mechanisms of deep brain stimulation". In: *Journal of Neurophysiology* 115 (1), pp. 19–38. ISSN: 15221598. DOI: 10.1152/JN.00281.2015/ASSET/IMAGES/LARGE/Z9K0011634190006. JPEG. URL: <https://journals.physiology.org/doi/abs/10.1152/jn.00281.2015>.
- Tong, Wei et al. (Mar. 2020). "Stimulation Strategies for Improving the Resolution of Retinal Prostheses". In: *Frontiers in Neuroscience* 14, p. 262. ISSN: 1662453X. DOI: 10.3389/FNINS.2020.00262/BIBTEX.
- Tresco, Patrick A. and Brent D. Winslow (2011). "The Challenge of Integrating Devices into the Central Nervous System". In: *Critical Reviews in Biomedical Engineering* 39 (1), pp. 29–44. ISSN: 0278-940X. DOI: 10.1615/CRITREVBIMEDENG.V39.I1.30. URL: <https://www.dl.begellhouse.com/journals/4b27cbfc562e21b8,7d5e987c7e576915,1e61f79c5183ad8b.html>.
- Saxena, Tarun et al. (July 2013). "The impact of chronic blood-brain barrier breach on intracortical electrode function". In: *Biomaterials* 34 (20), pp. 4703–4713. ISSN: 01429612. DOI: 10.1016/j.biomaterials.2013.03.007.
- Grill, Warren M., Sharon E. Norman, and Ravi V. Bellamkonda (July 2009). "Implanted Neural Interfaces: Biochallenges and Engineered Solutions". In: *Annual Review of Biomedical Engineering* 11, pp. 1–24. ISSN: 15239829. DOI: 10.1146/ANNUREV-BIOENG-061008-124927. URL: <https://www.annualreviews.org/doi/abs/10.1146/annurev-bioeng-061008-124927>.
- Polikov, Vadim S., Patrick A. Tresco, and William M. Reichert (Oct. 2005). "Response of brain tissue to chronically implanted neural electrodes". In: *Journal of Neuroscience Methods* 148 (1), pp. 1–18. ISSN: 0165-0270. DOI: 10.1016/J.JNEUMETH.2005.08.015.

- Zemelman, Boris V. et al. (Jan. 2002). "Selective photostimulation of genetically chARGed neurons". In: *Neuron* 33 (1), pp. 15–22. ISSN: 0896-6273. DOI: 10.1016/S0896-6273(01)00574-8. URL: <https://pubmed.ncbi.nlm.nih.gov/11779476/>.
- Boyden, Edward S. et al. (Aug. 2005). "Millisecond-timescale, genetically targeted optical control of neural activity". In: *Nature Neuroscience* 2005 8:9 8 (9), pp. 1263–1268. ISSN: 1546-1726. DOI: 10.1038/nn1525. URL: <https://www.nature.com/articles/nn1525>.
- Mendoza, Skyler D., Yasmine El-Shamayleh, and Gregory D. Horwitz (May 2017). "AAV-mediated delivery of optogenetic constructs to the macaque brain triggers humoral immune responses". In: *Journal of Neurophysiology* 117 (5), pp. 2004–2013. ISSN: 15221598. DOI: 10.1152/JN.00780.2016/ASSET/IMAGES/LARGE/Z9K0051740960006. JPEG. URL: <https://journals.physiology.org/doi/abs/10.1152/jn.00780.2016>.
- Stieglitz, T. et al. (Aug. 2002). "A biohybrid system to interface peripheral nerves after traumatic lesions: design of a high channel sieve electrode". In: *Biosensors and Bioelectronics* 17 (8), pp. 685–696. ISSN: 0956-5663. DOI: 10.1016/S0956-5663(02)00019-2.
- Rochford, Amy E. et al. (Apr. 2020). "When Bio Meets Technology: Biohybrid Neural Interfaces". In: *Advanced Materials* 32 (15), p. 1903182. ISSN: 1521-4095. DOI: 10.1002/ADMA.201903182. URL: <https://onlinelibrary.wiley.com/doi/full/10.1002/adma.201903182> <https://onlinelibrary.wiley.com/doi/abs/10.1002/adma.201903182>.
- Purcell, E. K. et al. (Mar. 2009). "In vivo evaluation of a neural stem cell-seeded prosthesis". In: *Journal of Neural Engineering* 6 (2), p. 026005. ISSN: 1741-2552. DOI: 10.1088/1741-2560/6/2/026005. URL: <https://iopscience.iop.org/article/10.1088/1741-2560/6/2/026005> <https://iopscience.iop.org/article/10.1088/1741-2560/6/2/026005/meta>.
- Faveri, Sara De et al. (Apr. 2014). "Bio-inspired hybrid microelectrodes: A hybrid solution to improve long-term performance of chronic intracortical implants". In: *Frontiers in Neuroengineering* 7 (APR), p. 7. ISSN: 16626443. DOI: 10.3389/FNENG.2014.00007/BIBTEX.
- Tang-Schomer, Min D. et al. (Apr. 2014). "Film-Based Implants for Supporting Neuron-Electrode Integrated Interfaces for The Brain". In: *Advanced Functional Materials* 24 (13), pp. 1938–1948. ISSN: 1616-3028. DOI: 10.1002/ADFM.201303196. URL: <https://onlinelibrary.wiley.com/doi/full/10.1002/adfm.201303196> <https://onlinelibrary.wiley.com/doi/abs/10.1002/adfm.201303196> <https://onlinelibrary.wiley.com/doi/10.1002/adfm.201303196>.
- Adewole, Dayo O. et al. (Jan. 2021). "Development of optically controlled "living electrodes" with long-projecting axon tracts for a synaptic brain-machine interface". In: *Science Advances* 7 (4). ISSN: 23752548. DOI: 10.1126/SCIADV.AAY5347/SUPPLFILE/AAY5347_SM.PDF. URL: <https://www.science.org/doi/abs/10.1126/sciadv.aay5347>.
- Bourne, Rupert R.A. et al. (Feb. 2021). "Trends in prevalence of blindness and distance and near vision impairment over 30 years: an analysis for the Global Burden of Disease Study". In: *The Lancet. Global health* 9 (2), e130–e143. ISSN: 2214-109X. DOI: 10.1016/S2214-109X(20)30425-3. URL: <https://pubmed.ncbi.nlm.nih.gov/33275950/>.
- Tybrandt, Klas et al. (Apr. 2018). "High-Density Stretchable Electrode Grids for Chronic Neural Recording". In: *Advanced Materials* 30 (15), p. 1706520. ISSN: 1521-4095. DOI:

- 10.1002/ADMA.201706520. URL: <https://onlinelibrary.wiley.com/doi/full/10.1002/adma.201706520>
- Douglas, R. J. and K. A. Martin (Aug. 1991). "A functional microcircuit for cat visual cortex". In: *The Journal of physiology* 440 (1), pp. 735–769. ISSN: 0022-3751. DOI: 10.1113/JPHYSIOL.1991.SP018733. URL: <https://pubmed.ncbi.nlm.nih.gov/1666655/>.
- Markram, Henry et al. (Jan. 1997). "Regulation of synaptic efficacy by coincidence of postsynaptic APs and EPSPs". In: *Science* 275 (5297), pp. 213–215. ISSN: 00368075. DOI: 10.1126/SCIENCE.275.5297.213
- Yamamoto, H. et al. (July 2016). "Unidirectional signal propagation in primary neurons micropatterned at a single-cell resolution". In: *Applied Physics Letters* 109 (4). ISSN: 00036951. DOI: 10.1063/1.4959836.
- Forró, Csaba et al. (Dec. 2018). "Modular microstructure design to build neuronal networks of defined functional connectivity". In: *Biosensors and Bioelectronics* 122, pp. 75–87. ISSN: 0956-5663. DOI: 10.1016/J.BIOS.2018.08.075.
- Millet, Larry J. and Martha U. Gillette (Dec. 2012). "New perspectives on neuronal development via microfluidic environments". In: *Trends in neurosciences* 35 (12), pp. 752–761. ISSN: 1878-108X. DOI: 10.1016/J.TINS.2012.09.001. URL: <https://pubmed.ncbi.nlm.nih.gov/23031246/>.
- Neto, Estrela et al. (Nov. 2016). "Compartmentalized Microfluidic Platforms: The Unrivaled Breakthrough of In Vitro Tools for Neurobiological Research". In: *The Journal of neuroscience : the official journal of the Society for Neuroscience* 36 (46), pp. 11573–11584. ISSN: 1529-2401. DOI: 10.1523/JNEUROSCI.1748-16.2016. URL: <https://pubmed.ncbi.nlm.nih.gov/27852766/>.
- Millet, Larry J. et al. (2007). "Microfluidic devices for culturing primary mammalian neurons at low densities". In: *Lab on a chip* 7 (8), pp. 987–994. ISSN: 1473-0197. DOI: 10.1039/B705266A. URL: <https://pubmed.ncbi.nlm.nih.gov/17653340/>.
- Francisco, Herbert et al. (Aug. 2007). "Regulation of Axon Guidance and Extension by 3-Dimensional Constraints". In: *Biomaterials* 28 (23), p. 3398. ISSN: 01429612. DOI: 10.1016/J.BIOMATERIALS.2007.04.015. URL: /pmc/articles/PMC1952179//pmc/articles/PMC1952179/?report=abstract
- Feber, Joost Le et al. (2015). "Barbed channels enhance unidirectional connectivity between neuronal networks cultured on multi electrode arrays". In: *Frontiers in Neuroscience* 9 (NOV), p. 412. ISSN: 1662453X. DOI: 10.3389/FNINS.2015.00412/BIBTEX.
- Peyrin, Jean Michel et al. (Oct. 2011). "Axon diodes for the reconstruction of oriented neuronal networks in microfluidic chambers". In: *Lab on a Chip* 11 (21), pp. 3663–3673. ISSN: 14730189. DOI: 10.1039/C1LC20014C. URL: <https://pubs.rsc.org/en/>

- content/articlehtml/2011/1c/c1lc20014chhttps://pubs.rsc.org/en/content/articlelanding/2011/1c/c1lc20014c.
- Pirlo, R. K. et al. (Mar. 2011). “Biochip/laser cell deposition system to assess polarized axonal growth from single neurons and neuron/glia pairs in microchannels with novel asymmetrical geometries”. In: *Biomicrofluidics* 5 (1), p. 013408. ISSN: 19321058. DOI: 10.1063/1.3552998. URL: <https://aip.scitation.org/doi/abs/10.1063/1.3552998>.
- Na, Sangcheol et al. (Mar. 2017). “Microfluidic neural axon diode”. In: *Technology* 04 (04), pp. 240–248. ISSN: 2339-5478. DOI: 10.1142/S2339547816500102.
- Renault, Renaud et al. (June 2016). “Asymmetric axonal edge guidance: a new paradigm for building oriented neuronal networks”. In: *Lab on a Chip* 16 (12), pp. 2188–2191. ISSN: 14730189. DOI: 10.1039/C6LC00479B. URL: <https://pubs.rsc.org/en/content/articlehtml/2016/1c/c6lc00479bhttps://pubs.rsc.org/en/content/articlelanding/2016/1c/c6lc00479b>.
- Holloway, Paul M. et al. (Apr. 2019). “Asymmetric confinement for defining outgrowth directionality”. In: *Lab on a Chip* 19 (8), pp. 1484–1489. ISSN: 1473-0189. DOI: 10.1039/C9LC00078J. URL: <https://pubs.rsc.org/en/content/articlehtml/2019/1c/c9lc00078jhttps://pubs.rsc.org/en/content/articlelanding/2019/1c/c9lc00078j>.
- Gladkov, Arseniy et al. (Nov. 2017). “Design of Cultured Neuron Networks in vitro with Predefined Connectivity Using Asymmetric Microfluidic Channels”. In: *Scientific Reports* 2017 7:1 7 (1), pp. 1–14. ISSN: 2045-2322. DOI: 10.1038/s41598-017-15506-2. URL: <https://www.nature.com/articles/s41598-017-15506-2>.
- Isomura, Takuya et al. (Nov. 2015). “Signal transfer within a cultured asymmetric cortical neuron circuit”. In: *Journal of Neural Engineering* 12 (6), p. 066023. ISSN: 1741-2552. DOI: 10.1088/1741-2560/12/6/066023. URL: <https://iopscience.iop.org/article/10.1088/1741-2560/12/6/066023https://iopscience.iop.org/article/10.1088/1741-2560/12/6/066023/meta>.
- Braso, Guillem and Laura Leal-Taixe (Dec. 2019). “Learning a Neural Solver for Multiple Object Tracking”. In: *Proceedings of the IEEE Computer Society Conference on Computer Vision and Pattern Recognition*, pp. 6246–6256. ISSN: 10636919. DOI: 10.1109/CVPR42600.2020.00628. URL: <https://arxiv.org/abs/1912.07515v2>.
- Krizhevsky, Alex, Ilya Sutskever, and Geoffrey E Hinton (2012). “ImageNet Classification with Deep Convolutional Neural Networks”. In: ed. by F Pereira et al. Vol. 25. Curran Associates, Inc. URL: <https://proceedings.neurips.cc/paper/2012/file/c399862d3b9d6b76c8436e924a68c45b-Paper.pdf>.
- Girshick, Ross et al. (Nov. 2013). “Rich feature hierarchies for accurate object detection and semantic segmentation”. In: *arXiv*. URL: <https://arxiv.org/abs/1311.2524>.
- Girshick, Ross (Apr. 2015). “Fast R-CNN”. In: *arXiv*. URL: <https://arxiv.org/abs/1504.08083>.
- Ren, Shaoqing et al. (June 2015). “Faster R-CNN: Towards Real-Time Object Detection with Region Proposal Networks”. In: *arXiv*. URL: <https://arxiv.org/abs/1506.01497>.
- Redmon, Joseph et al. (June 2015). “You Only Look Once: Unified, Real-Time Object Detection”. In: *Proceedings of the IEEE Computer Society Conference on Computer Vision and Pattern Recognition* 2016-December, pp. 779–788. ISSN: 10636919. DOI: 10.1109/CVPR.2016.91. URL: <https://arxiv.org/abs/1506.02640v5>.

- Redmon, Joseph and Ali Farhadi (Apr. 2018). “YOLOv3: An Incremental Improvement”. In: *arXiv*. URL: <https://arxiv.org/abs/1804.02767>.
- Long, Xiang et al. (July 2020). “PP-YOLO: An Effective and Efficient Implementation of Object Detector”. In: *arXiv*. URL: <http://arxiv.org/abs/2007.12099>.
- Bewley, Alex et al. (Aug. 2016). “Simple online and realtime tracking”. In: *Proceedings - International Conference on Image Processing, ICIP* 2016-August, pp. 3464–3468. ISSN: 15224880. DOI: [10.1109/ICIP.2016.7533003](https://doi.org/10.1109/ICIP.2016.7533003).
- Kuhn, Harold W (Mar. 1955). “The Hungarian Method for the Assignment Problem”. In: *Naval Research Logistics Quarterly* 2 (1–2), pp. 83–97. DOI: [10.1002/nav.3800020109](https://doi.org/10.1002/nav.3800020109).
- Wang, Congchao, Yizhi Wang, and Guoqiang Yu (Nov. 2019). “Efficient Global Multi-object Tracking Under Minimum-cost Circulation Framework”. In: *IEEE Transactions on Pattern Analysis and Machine Intelligence*, pp. 1–1. ISSN: 0162-8828. DOI: [10.1109/tpami.2020.3026257](https://doi.org/10.1109/tpami.2020.3026257). URL: <https://arxiv.org/abs/1911.00796v2>.
- Wojke, Nicolai, Alex Bewley, and Dietrich Paulus (Mar. 2017). “Simple Online and Real-time Tracking with a Deep Association Metric”. In: *Proceedings - International Conference on Image Processing, ICIP* 2017-September, pp. 3645–3649. ISSN: 15224880. DOI: [10.1109/ICIP.2017.8296962](https://doi.org/10.1109/ICIP.2017.8296962). URL: <https://arxiv.org/abs/1703.07402v1>.
- Yoon, Kwangjin et al. (Jan. 2019). “Data Association for Multi-Object Tracking via Deep Neural Networks”. In: *Sensors 2019, Vol. 19, Page 559* 19 (3), p. 559. ISSN: 14248220. DOI: [10.3390/S19030559](https://doi.org/10.3390/S19030559). URL: <https://www.mdpi.com/1424-8220/19/3/559>.
- Tsai, Hsieh Fu et al. (Jan. 2019). “Usiigaci: Instance-aware cell tracking in stain-free phase contrast microscopy enabled by machine learning”. In: *SoftwareX* 9, pp. 230–237. ISSN: 2352-7110. DOI: [10.1016/J.SOFTX.2019.02.007](https://doi.org/10.1016/J.SOFTX.2019.02.007).
- Anjum, Samreen and Danna Gurari (June 2020). “CTMC: Cell tracking with mitosis detection dataset challenge”. In: *IEEE Computer Society Conference on Computer Vision and Pattern Recognition Workshops* 2020-June, pp. 4228–4237. ISSN: 21607516. DOI: [10.1109/CVPRW50498.2020.00499](https://doi.org/10.1109/CVPRW50498.2020.00499).
- Welshans, Kristy and Gary J. Bassell (July 2011). “Netrin-1-Induced Local β -Actin Synthesis and Growth Cone Guidance Requires Zipcode Binding Protein 1”. In: *Journal of Neuroscience* 31 (27), pp. 9800–9813. ISSN: 0270-6474. DOI: [10.1523/JNEUROSCI.0166-11.2011](https://doi.org/10.1523/JNEUROSCI.0166-11.2011). URL: <https://www.jneurosci.org/content/31/27/9800>.
- Sofroniew, Nicholas et al. (Oct. 2021). “napari/napari: 0.4.12rc2”. In: DOI: [10.5281/ZENODO.5587893](https://doi.org/10.5281/ZENODO.5587893). URL: <https://zenodo.org/record/5587893>.
- Ioffe, Sergey and Christian Szegedy (Feb. 2015). “Batch Normalization: Accelerating Deep Network Training by Reducing Internal Covariate Shift”. In: *32nd International Conference on Machine Learning, ICML 2015* 1, pp. 448–456. URL: <https://arxiv.org/abs/1502.03167v3>.
- Maas, Andrew L, Awni Y Hannun, and Andrew Y Ng (2013). “Rectifier nonlinearities improve neural network acoustic models”. In.
- Bodla, Navaneeth et al. (Apr. 2017). “Soft-NMS – Improving Object Detection With One Line of Code”. In: *Proceedings of the IEEE International Conference on Computer Vision* 2017-October, pp. 5562–5570. ISSN: 15505499. DOI: [10.1109/ICCV.2017.593](https://doi.org/10.1109/ICCV.2017.593). URL: <https://arxiv.org/abs/1704.04503v2>.

- Kingma, Diederik P. and Jimmy Lei Ba (Dec. 2014). “Adam: A Method for Stochastic Optimization”. In: *3rd International Conference on Learning Representations, ICLR 2015 - Conference Track Proceedings*. URL: <https://arxiv.org/abs/1412.6980v9>.
- Hart, Peter E., Nils J. Nilsson, and Bertram Raphael (1968). “A Formal Basis for the Heuristic Determination of Minimum Cost Paths”. In: *IEEE Transactions on Systems Science and Cybernetics* 4 (2), pp. 100–107. ISSN: 21682887. DOI: 10.1109/TSSC.1968.300136.
- Leal-Taixé, Laura et al. (Apr. 2015). “MOTChallenge 2015: Towards a Benchmark for Multi-Target Tracking”. In: *ArXiv*. URL: <https://arxiv.org/abs/1504.01942v1>.
- Azulay, Aharon and Yair Weiss (May 2018). “Why do deep convolutional networks generalize so poorly to small image transformations?” In: *arXiv*. URL: <https://arxiv.org/abs/1805.12177>.
- Keenan, Thomas M. et al. (Mar. 2006). “Automated identification of axonal growth cones in time-lapse image sequences”. In: *Journal of neuroscience methods* 151 (2), pp. 232–238. ISSN: 01650270. DOI: 10.1016/J.JNEUMETH.2005.07.010. URL: [/pmc/articles/PMC3848907/](https://pmc/articles/PMC3848907/)?report=abstract<https://www.ncbi.nlm.nih.gov/pmc/articles/PMC3848907/>.
- Liu, Zewen, Timothy Cootes, and Christoph Ballestrem (Oct. 2020). “An End to End System for Measuring Axon Growth”. In: *Lecture Notes in Computer Science (including subseries Lecture Notes in Artificial Intelligence and Lecture Notes in Bioinformatics)* 12436 LNCS, pp. 455–464. ISSN: 16113349. DOI: 10.1007/978-3-030-59861-7_46. URL: https://link.springer.com/chapter/10.1007/978-3-030-59861-7_46.
- Funke, Jan et al. (July 2019). “Large Scale Image Segmentation with Structured Loss Based Deep Learning for Connectome Reconstruction”. In: *IEEE transactions on pattern analysis and machine intelligence* 41 (7), pp. 1669–1680. ISSN: 1939-3539. DOI: 10.1109/TPAMI.2018.2835450. URL: <https://pubmed.ncbi.nlm.nih.gov/29993708/>?report=Abstract[https://pubmed.ncbi.nlm.nih.gov/29993708/?dopt=Abstract](https://pubmed.ncbi.nlm.nih.gov/29993708/).
- Abdollahzadeh, Ali et al. (Feb. 2021). “DeepACSON automated segmentation of white matter in 3D electron microscopy”. In: *Communications Biology* 2021 4:1 4 (1), pp. 1–14. ISSN: 2399-3642. DOI: 10.1038/s42003-021-01699-w. URL: <https://www.nature.com/articles/s42003-021-01699-w>.